

1

2       **Effects of transport on a biomass burning plume from Indochina**  
3                       **during EMeRGe-Asia identified by WRF-Chem**

4

5       **Chuan-Yao Lin<sup>1\*</sup>, Wan-Chin Chen<sup>1</sup>, Yi-Yun Chien<sup>1</sup>, Charles C. K. Chou<sup>1</sup>, Chian-**  
6       **Yi Liu<sup>1</sup>, Helmut Ziereis<sup>2</sup>, Hans Schlager<sup>2</sup>, Eric Förster<sup>3</sup>, Florian Obsersteiner<sup>3</sup>,**  
7       **Ovid O. Krüger<sup>4</sup>, Bruna A. Holanda<sup>4</sup>, Mira L. Pöhlker<sup>4,a</sup>, Katharina Kaiser<sup>5,7</sup>,**  
8       **Johannes Schneider<sup>5</sup>, Birger Bohn<sup>8</sup>, Klaus Pfeilsticker<sup>9,10</sup>, Benjamin Weyland<sup>10</sup>,**  
9       **Maria Dolores Andrés Hernández<sup>6</sup>, John P. Burrows<sup>6</sup>**

10

- 11       1. Research Center for Environmental Changes, Academia Sinica, Taipei, Taiwan  
12       2. Deutsches Zentrum für Luft- und Raumfahrt (DLR), Institut für Physik der  
13       Atmosphäre, Oberpfaffenhofen, Germany  
14       3. Karlsruhe Institute of Technology, Institute of Meteorology and Climate Research,  
15       Karlsruhe, Germany  
16       4. Multiphase Chemistry Department, Max Planck Institute for Chemistry, Mainz,  
17       Germany  
18       5. Particle Chemistry Department, Max Planck Institute for Chemistry, Mainz,  
19       Germany  
20       6. Institute of Environmental Physics, University Bremen, Bremen, Germany  
21       7. Institute for Atmospheric Physics, Johannes Gutenberg University, Mainz,  
22       Germany  
23       8. Institute of Energy and Climate Research IEK-8, Forschungszentrum Jülich, Jülich,  
24       Germany  
25       9. Heidelberg Center for the Environment, Heidelberg University, Heidelberg,  
26       Germany  
27       10. Institute of Environmental Physics, Heidelberg University, Heidelberg, Germany

28       <sup>a</sup>now at: Faculty of Physics and Earth Sciences · Leipzig Institute for Meteorology,  
29       University of Leipzig/Experimental Aerosol and Cloud Microphysics Department,  
30       Leibniz Institute for Tropospheric Research, Leipzig, Germany

31

32       \*Corresponding author

33       **Chuan Yao Lin,**

34       Research Center for Environmental Changes, Academia Sinica, Taipei, Taiwan

35       128 Sec. 2, Academia Rd, Nankang, Taipei 115, Taiwan

36       (E-mail: [yao435@rcec.sinica.edu.tw](mailto:yao435@rcec.sinica.edu.tw), Tel.: +886-2-27875892, Fax: +886-2-27833584),

37 **Abstract.**

38 The Indochina biomass burning (BB) season in springtime has a substantial  
39 environmental impact on the surrounding areas in Asia. In this study, we evaluated the  
40 environmental impact of a major long-range BB transport event on 19 March 2018 (a  
41 flight of the HALO research aircraft, flight F0319) preceded by a minor event on 17  
42 March 2018 (flight F0317). Aircraft data obtained during the campaign in Asia of the  
43 Effect of Megacities on the transport and transformation of pollutants on the Regional  
44 to Global scales (EMeRGe) were available between 12 March and 7 April 2018. In the  
45 F0319, results of 1-min mean carbon monoxide (CO), ozone (O<sub>3</sub>), acetone (ACE),  
46 acetonitrile (ACN), organic aerosol (OA) and black carbon aerosol (BC) concentrations  
47 were up to 312.0 ppb, 79.0 ppb, 3.0 ppb, 0.6 ppb, 6.4 μg m<sup>-3</sup>, 2.5 μg m<sup>-3</sup> respectively,  
48 during the flight, which passed through the BB plume transport layer (BPTL) between  
49 the elevation of 2000–4000 m over the East China Sea (ECS). During F0319, CO, O<sub>3</sub>,  
50 ACE, ACN, OA and BC maximum of the 1 minute average concentrations were higher  
51 in the BPTL by 109.0 ppb, 8.0 ppb, 1.0 ppb, 0.3 ppb, 3.0 μg m<sup>-3</sup> and 1.3 μg m<sup>-3</sup>  
52 compared to flight F0317, respectively. Sulfate aerosol, rather than OA, showed the  
53 highest concentration at low altitudes (<1000 m) in both flights F0317 and F0319  
54 resulting from the continental outflow in the ECS.

55 The transport of BB aerosols from Indochina and its impacts on the downstream  
56 area was evaluated using a WRF-Chem model. **The modeling results tended to**  
57 **overestimate the concentration of the species, with examples being CO (64 ppb), OA**  
58 **(0.3 μg m<sup>-3</sup>), BC (0.2 μg m<sup>-3</sup>) and O<sub>3</sub> (12.5 ppb) in the BPTL.** Over the ECS, the  
59 simulated BB contribution demonstrated an increasing trend from the lowest values on  
60 17 March 2018 to the highest values on 18 and 19 March 2018 for CO, fine particulate  
61 matter (PM<sub>2.5</sub>), OA, BC, hydroxyl radicals (OH), nitrogen oxides (NO<sub>x</sub>), total reactive  
62 nitrogen (NO<sub>y</sub>), and O<sub>3</sub>; by contrast, the variation of J(O<sup>1</sup>D) decreased as the BB

63 plume's contribution increased over the ECS. In the low boundary layer (<1000 m), the  
64 BB plume's contribution to most species in the remote downstream areas was <20 %.  
65 However, at the BPTL, the contribution of the long-range transported BB plume was as  
66 high as 30–80 % for most of the species ( $\text{NO}_y$ ,  $\text{NO}_x$ ,  $\text{PM}_{2.5}$ , BC, OH,  $\text{O}_3$ , and CO) over  
67 South China (SC), Taiwan, and the ECS. BB aerosols were identified as a potential  
68 source of cloud condensation nuclei, and the simulation results indicated that the  
69 transported BB plume had an effect on cloud water formation over SC and the ECS on  
70 19 March 2018. The combination of BB aerosol enhancement with cloud water resulted  
71 in a reduction of incoming shortwave radiation at the surface in SC and the ECS which  
72 potentially has significant regional climate implications.

73

74

## 75 **1 Introduction**

76 Biomass burning (BB) is one of the main sources of aerosols, greenhouse gases, and air  
77 pollutants (e.g. Ramanathan et al., 2007; Lin et al., 2009; 2014; Tang, 2003; Carmichael  
78 et al., 2003; Chi et al., 2010; Fu et al., 2012; Lin N.H. et al., 2012; Chuang et al., 2016).  
79 Reid et al. (2013) and Giglio et al. (2013) investigated the seasonal aerosol optical depth  
80 over Southeast Asia and have indicated that Indochina is a major contributor of carbon  
81 emissions in springtime. Galanter et al. (2000) estimated that BB accounts for 15–30 %  
82 of the entire tropospheric CO background. Huang et al. (2013) indicated that the  
83 contribution of BB in Southeast Asia to the aerosol optical depth (AOD) in Hong Kong  
84 and Taiwan could be in the range of 26–62 %. Moreover, BB emissions over Indochina  
85 are a significant contributor to black carbon (BC), organic carbon (OC), and  $\text{O}_3$  in East  
86 Asia (Lin et al., 2014). In their BB modeling study, Lin et al. (2014) identified a  
87 northeast (NE) to southwest (SW) zone stretching from South China (SC) to Taiwan  
88 with a reduction in shortwave radiation of approximately  $20 \text{ W m}^{-2}$  at the ground

89 surface. In addition, the total carbon emission from BB in Southeast Asia is  
90 approximately 91 Tg C yr<sup>-1</sup>, accounting for 4.9 % of the global total (Yadav et al.,  
91 2017). According to Xu et al. (2018), BB in Indochina leads to BC production at high  
92 concentrations of up to 2–6 μg m<sup>-3</sup> in spring. The authors reported that BC particles  
93 were transported to the glaciers in the Tibetan Plateau, where it significantly affected  
94 the melting of the snow, causing some severe environmental problems, such as water  
95 resource depletion. Ding et al. (2021) indicated that BB aloft aerosols strongly increase  
96 the low cloud coverage over both land and ocean and affect the monsoon in the  
97 subtropical Southeast Asia.

98 Although many researchers have indicated the importance of BB emissions, their  
99 precise estimation and applying in the modeling study remains challenging (Fu et al.  
100 2012; Huang et al. 2013; Pimonstree et al. 2018; Marvin et al. 2021). For example,  
101 Heald et al. (2003) conducted an emission inventory in Southeast Asia and reported that  
102 the uncertainties of BB emission estimations could be a factor of three or even higher.  
103 Following an inverse model analysis, Palmer et al. (2003) also indicated the  
104 overestimation of regional BB emissions over Indochina. **Shi and Yamaguchi (2014)**  
105 **pointed out BB emissions exhibited strong temporal interannual variability between**  
106 **2001 and 2010 over southeast Asia.** Satellite data can be used to easily locate hotspots  
107 such as those where agricultural residuals burning and forest wildfires are occurring  
108 worldwide. However, accurately quantifying the amount of BB emission from satellite  
109 data is difficult because anthropogenic pollutants and BB emissions are typically mixed  
110 in the atmosphere. During the NASA Transport and Chemical Evolution over the  
111 Pacific (TRACE-P) aircraft mission in spring 2001, Jacob et al. (2003) observed that  
112 warm conveyor belts (WCBs) lift both anthropogenic and BB (from SE Asia) air  
113 pollution to the free troposphere, resulting in complex chemical signatures.  
114 Wiedinmyer et al. (2011) demonstrated that the uncertainty of emission estimation

115 could be as high as a factor of 2 because of the error introduced by estimates in fire  
116 hotspots, area burned, land cover maps, biomass consumption, and emission factors in  
117 the model. In this context, Lin et al. (2014) highlighted the uncertainty of emission  
118 estimation in the first version of Fire Inventory from NCAR (Wiedinmyer et al., 2011).

119 The transport of BB pollution is strongly dependent on the atmospheric structure  
120 and weather conditions. Tang et al. (2003) noted that most BB aerosols, having their  
121 source in Indochina (mainly south of 25 °N and be alofted to an altitude of 2000–4000  
122 m) during the TRACE-P campaign were associated with outflow in the WCB region  
123 after frontal passage. Lin et al. (2009) suggested a mountain lee-side troughs as an  
124 important mechanism, resulting in BB product transport from the surface to >3000 m.  
125 BB pollution is often transported from its sources to the East China Sea (ECS), Taiwan,  
126 and the western North Pacific within a few days.

127 The airborne field experiment EMeRGe ( Effect of Megacities on the transport and  
128 transformation of pollutants on the Regional to Global scales) over Asia was led by the  
129 University of Bremen, Germany and conducted in collaboration with Academia Sinica,  
130 during the inter-monsoon period in 2018 ([http://www.iup.uni-](http://www.iup.uni-bremen.de/emerge/home/home.html)  
131 [bremen.de/emerge/home/home.html](http://www.iup.uni-bremen.de/emerge/home/home.html)). The EMeRGe aircraft mission consists of two  
132 parts. The first mission phase was conducted in Germany in July 2017 and the second  
133 phase was conducted from Taiwan in 2018 (Andrés Hernández et al. 2022).EMeRGe in  
134 Asia aimed at the investigation of the long range transport (LRT) of local and regional  
135 pollution originating in Asian major population centers (MPCs) from the Asian  
136 continent into the Pacific. A central part of the project was the airborne measurement  
137 of pollution plumes on-board of the High Altitude and Long Range Research Aircraft  
138 (HALO). The HALO platform was based in Tainan, Taiwan (Fig. 1a-b), and made  
139 optimized transects and vertical profiling in regions north or south of Taiwan,  
140 dependent on the relevant weather and emission conditions. HALO measurements

141 additionally provide important information for the evaluation of the LRT of BB  
142 emissions and its potential environmental impact in East Asia between 12 March and 7  
143 April 2018. During the EMeRGe-Asia campaign, HALO carried out 12 mission flights  
144 in Asia and 4 transfer flights from Europe to Asia with a total of 110 flight hours.

145 This paper is organized as follows: the model configuration and BB emission  
146 analysis employed in the model simulation are described in Section 2, and the weather  
147 conditions and HALO measurement results are presented in Section 3. The model  
148 performance, as well as the evaluation of BB product transport and effects on East Asia  
149 selected regions are discussed in Sections 4 and 5, respectively.

150

## 151 **2 Aircraft data and Model configuration**

### 152 **2.1 HALO aircraft data**

153 The HALO aircraft was equipped with a number of instruments and a detailed  
154 description of the measurement systems onboard the HALO was presented in Andrés  
155 Hernández et al.(2022). In this study, aerosol data (OA, BC,  $\text{SO}_4^{2-}$ ,  $\text{NO}_3^-$ ,  $\text{NH}_4^+$ ), and  
156 trace gases such as CO,  $\text{SO}_2$ ,  $\text{O}_3$ ,  $\text{NO}_x$ ,  $\text{NO}_y$ , acetone (ACE), acetonitrile (ACN), HCHO,  
157 HONO, and photolysis rate  $J(\text{O}^1\text{D})$ ,  $J(\text{NO}_2)$  were employed in the analysis.

### 158 **2.2 WRF-Chem Model and model configuration**

159 We used the Weather Research Forecasting with Chemistry (WRF-Chem) model (Ver.  
160 4.1.1) (Grell et al., 2005; Powers et al. 2017) to study the LRT of air masses associated  
161 with BB pollutants in Indochina. The initial and boundary meteorological conditions  
162 for WRF-Chem were obtained from National Centers for Environmental Prediction  
163 (NCEP)-GDAS Global Analysis data sets at 6-h intervals. The Mellor–Yamada–Janjic  
164 planetary boundary layer scheme (Janjic, 1994) was applied. The horizontal resolution  
165 for the simulations performed was 10 km, and the grid box had  $442 \times 391$  points in the  
166 east–west and north–south directions (Fig. 1a). A total of 41 vertical levels were

167 included, with the lowest level at an elevation of approximately 50 m. To improve the  
168 accuracy of the meteorological fields, a grid nudging four-dimensional data  
169 assimilation scheme was applied using the NCEP-GDAS Global Analysis data.

170 The cloud microphysics used followed the Lin scheme (Morrison et al., 2005). The  
171 rapid radiative transfer model (Zhao et al., 2011) was used for both longwave and  
172 shortwave radiation schemes. Moreover, land surface processes are simulated using the  
173 Noah-LSM scheme (Hong et al., 2009). In terms of transport processes, we considered  
174 advection by winds, convection by clouds, and diffusion by turbulent mixing. The  
175 removal processes in this study were gravitational settling, surface deposition, and wet  
176 deposition (scavenging in convective updrafts and rainout or washout in large-scale  
177 precipitation). The kinetic preprocessor (KPP) interface was used in both of the  
178 chemistry schemes of the Regional Atmospheric Chemistry Mechanism (RACM,  
179 Stockwell et al., 1990). The secondary organic aerosol formation module, the Modal  
180 Aerosol Dynamics Model for Europe (Ackermann et al., 1998)/Volatility Basis Set  
181 (Ahmadov et al., 2012), was also employed in the WRF-Chem model. **In RACM, the**  
182 **“KET” represents acetone and higher saturated ketones (KET) (Stockwell et al. 1997).**  
183 **According to Singh et al. (1994), BB and the primary anthropogenic emissions could**  
184 **contribute 26% and 3%, respectively, to the atmospheric acetone sources. The model**  
185 **configuration and physics and chemistry options are listed in Table 1.**

186

### 187 **2.3 Emission Inventories**

188 Anthropogenic emissions, such as NO<sub>x</sub>, CO, SO<sub>2</sub>, nonmethane volatile organic  
189 compounds, sulfate, nitrate, PM<sub>10</sub>, and PM<sub>2.5</sub>, were adopted on the basis of the emission  
190 **inventory in Asia – MICS-Asia III which is the year in 2010 (Li et al., 2020; Kong et**  
191 **al., 2020). For BB emissions FINNv1.5 (<https://www.acom.ucar.edu/Data/fire/>) was**  
192 **employed.** FINN provided daily, 1000 m resolution, global estimates of the trace gas

193 and particle emissions from open BB, which included wildfires, agricultural fires, and  
194 prescribed burning but not biofuel use and trash burning (Wiedinmyer et al., 2011). **The**  
195 **anthropogenic emissions in Taiwan were obtained from the Taiwan Emission Data**  
196 **System (TEDS) which is the emission inventory of the air-pollutant monitoring**  
197 **database of the Taiwan Environmental Protection Administration. The TEDS version**  
198 **used for this study was V9.0 (2013)** and contained data on eight primary atmospheric  
199 pollutants: CO, NO, NO<sub>2</sub>, NO<sub>x</sub>, O<sub>3</sub>, PM<sub>10</sub>, PM<sub>2.5</sub>, and SO<sub>2</sub>.

200

### 201 **3 Characteristics of the field experiment**

#### 202 **3.1 MODIS Aerosol optical depth and Weather conditions**

203 Figures 2a and b visualizes the numerous fire hotspots and high aerosol optical depth  
204 on 17 March 2018 registered by the MODIS satellite. Indeed, a large number of BB fire  
205 hotspots frequently occurred over Indochina during the springtime (Lin et al. 2009;  
206 2014) and EMERGe-Asia campaign (Supplementary Figure S1). On 17 March 2018 at  
207 06:00 UTC (14:00 LT; LT = UTC+8:00) the weather data indicated a series of high-  
208 **pressure systems in northern China and a separate high-pressure system over the Japan**  
209 **sea (Fig. 2c)**. At 1000 hPa, a strong northerly continental outflow was identified over  
210 southern Japan, the ECS, and Taiwan (Fig. 2d). On 19 March 2018, a new frontal  
211 system was located from Korea to the Guangdong province in SC (Fig. 2e). On the  
212 same day at 06:00 UTC, a discontinued flow was identified at the frontal zone to the  
213 north of Taiwan in the ECS (Fig. 2f). In other words, Taiwan was located at the  
214 prefrontal and warm conveyor area due to the surrounding southerly flow on 19 March  
215 2018 at 06:00 UTC (Figs. 2e and 2f, respectively). The southerly wind was gradually  
216 replaced by the northeasterly after another frontal passage on 20 March 2018 at 00:00  
217 UTC (data not shown).

218 In the upper layer (700 hPa; Figs. 2g–2j), the flow pattern differed from that at the



219 near-ground surface (1000 hPa; Figs. 2d and 2f). A southwesterly strong wind, coming  
220 from the east side of the Tibetan Plateau in SC, moving to the North Eats i.e. Korea, is  
221 converted to a polar front wave flow in northeastern China and Korea on 17 March  
222 2018 (Fig. 2g). This high-elevation northward strong wind belt distribution at 700 hPa  
223 was associated with a corresponding lee-side trough at the east of the Tibetan Plateau,  
224 whereas a ridge was noted over the east coast of China on the same day (Fig. 2h).  
225 Consistent with the mechanism reported by Lin et al. (2009), once a significant lee-side  
226 trough formed, it provided favorable conditions for the upward motion over the lee-side  
227 of the Tibetan Plateau and brought BB emission to the free troposphere layer following  
228 the strong wind belt transport to the downwind area. After the weather system moved  
229 to the east, the north–south trough turned to SW–NE such that the strong wind belt was  
230 in an approximately SW–NE direction and located between 20 and 30 °N on 19 March  
231 2018 (Figs. 2i and 2j). In conclusion, the Indochina BB pollutants were driven by the  
232 strong wind belt from Indochina, northward to SC on 17 March 2018 and then eastward  
233 passing over Taiwan between 20 and 30 °N to the south of Japan on 19 March 2018.

### 234 **3.2 Characteristics of LRT BB to the ECS by WRF-Chem model**

235 Figure 3 shows latitude longitude plots of the simulated CO concentration  
236 differences with and without BB emission at an elevation of 1000 m (Fig. 3a), mainly  
237 in Indochina, SC, and the South China Sea on 17 March 2018. The ambient flow was  
238 easterly and then northward from the South China Sea to SC at 1000 m elevation  
239 between 00:00 and 12:00 UTC on 17 March 2018 (Fig. 3a-b). The BB plume  
240 accumulated and persisted for an extended period in the lower part of the boundary  
241 layer on 17 and 19 March 2018 (Figs. 3a-b, and 3e-f). In contrast, the high CO  
242 concentration followed the southwesterly or westerly strong wind belt (Figs. 3c-d, and  
243 3g-h) and its weather conditions (Fig. 2) at an elevation of 3000-m (700 hPa). Following  
244 the movement of the ridge and trough at the 700 hPa geopotential height (Fig. 2h and

245 2j), the associated strong wind belt turned to move eastward in the SW–NE direction  
246 between 17 and 19 March 2018. The BB plume transport over Indochina was affected  
247 by a fast-moving strong flow at 700 hPa (Fig. 2g and 2i), shifting the plume toward  
248 Taiwan and the ECS, during 17–19 March 2018. The highest CO concentration  
249 contributed by the BB plume was >150 ppb, originally sourced from Indochina, and it  
250 was mainly transported northward on 17 March 2018 (Figs. 3c-d) and then covered a  
251 large area in East Asia at a CO concentration of >100 ppb on 19 March 2018 (Figs. 3g-  
252 h). Figure 4 indicates simulation differences for the contribution of BB along an E–W  
253 cross-section at 30 °N at 16:00 UTC on 18 March 2018 (Fig. 4a) and 06:00 UTC on 19  
254 March 2018 (Fig. 4b). We noted that a strong wind at 2000 m elevation and a high CO  
255 concentration (>70 ppb) due to BB at the BPTL. Moreover, the CO concentration  
256 attributed to BB was low at the elevation of >4000 m on 19 March at 06:00 UTC (Fig.  
257 4b), showing that the BB pollutants mainly affect altitudes below 4000 m.

### 258 **3.3 Aircraft measurements**

259 Two HALO flights were scheduled to the ECS to measure the pollutants following the  
260 continental outflow; the flights departed on 17 (Fig. 5a) and 19 (Fig. 6a) March 2018  
261 and followed similar tracks. To indicate the measurement results along the flight path,  
262 the 1-min average data is shown in Figures 5b and 6b. On 17 March 2018, the flight  
263 departed from Tainan (Fig. 1b) at 01:09 UTC (09:09 LT) first southbound and then  
264 northward to the ECS (Fig. 5a). The elevation for sample collection was mainly <4000  
265 m, where the CO concentration was found to be <200 ppb in most cases on that day  
266 (Fig. 5b). At elevations between 2000 and 4000 m, the concentration of the major  
267 aerosol components (i.e., OA, BC,  $\text{SO}_4^{2-}$ ,  $\text{NO}_3^-$ , and  $\text{NH}_4^+$ ) was mostly <2  $\mu\text{g m}^{-3}$ ,  
268 except just above western Taiwan after 08:00 UTC (Figs. 5a–5d). The peak  
269 concentrations for OA, BC,  $\text{SO}_4^{2-}$ ,  $\text{NH}_4^+$ , and  $\text{NO}_3^-$  were 3.4, 1.2, 2.1, and 0.7  $\mu\text{g m}^{-3}$ ,  
270 respectively, at the altitude between 2000 and 4000 m.  $\text{SO}_4^{2-}$  demonstrated the highest

271 concentration among the aerosol components, especially during 04:00–04:37 and  
272 05:48–06:15 UTC (peaking at  $5.1 \mu\text{g m}^{-3}$ ) when the flight was north of  $30^\circ\text{N}$  and an  
273 elevation of  $<1000 \text{ m}$  (Figs. 5a–5c). This result could be attributed to anthropogenic  
274 pollution from the continental outflow (Lin et al. 2012) or probably part from Japan  
275 contributed to the high sulfate concentration in the boundary layer over the ECS. As for  
276 the trace gases such as ACE, ACN and  $\text{O}_3$ , their concentrations between 2000 and 4000  
277 m were ranging between 1–2 ppb, 0.1–0.3 ppb, and 60–70 ppb (Fig. 5b), respectively,  
278 implying minor influence over the ECS by the BB plume in this flight. Figure 5e  
279 illustrates the HYSPLIT (Stein et al., 2021) 96-h backward trajectories, which  
280 identified the air mass origin starting at 02:00 UTC, followed by 04:00, 06:00, and  
281 09:00 UTC. The continental outflow contributed to higher sulfate concentrations (3–5  
282  $\mu\text{g m}^{-3}$  at  $33^\circ\text{N}$ ) at 04:00 and 06:00 UTC (Figs. 5b, 5c, and 5e) at  $<1000 \text{ m}$  along the  
283 flight path. In contrast, south of  $25^\circ\text{N}$  and above Taiwan, the local pollution and  
284 continental outflow are dominating sources on 17 March 2018.

285 The HALO flight on 19 March 2018 departed at 00:19 UTC (08:19 LT). It was  
286 bound northward and sampled air at an altitude of  $<4000 \text{ m}$  most of the time, as shown  
287 in Figures 6a and 6b. Figures 6c and 6d indicate the latitude-height variation of  $\text{SO}_4^{2-}$   
288 and OA mass concentrations along the flight path on 19 March 2018. As the flight left  
289 Taiwan, it maintained an elevation of  $3000 \text{ m}$  during 01:00–02:00 UTC (Fig. 6a,  $121^\circ\text{E}$ –  
290  $126^\circ\text{E}$ ) and then descended to  $<1000 \text{ m}$  during 02:00–02:40 UTC (Fig. 6b). The OA  
291 mass concentration was higher at  $3000 \text{ m}$  than at the low altitude during 01:00–03:00  
292 UTC (Figs. 6b and 6d). In particular, CO, OA and BC exhibited a substantial peak  
293 concentration of 312 ppb,  $6.4 \mu\text{g m}^{-3}$  and  $2.5 \mu\text{g m}^{-3}$  at 01:54 and 02:51 UTC at  $26^\circ\text{N}$ ,  
294  $125^\circ\text{E}$ – $126^\circ\text{E}$ , and an altitude of  $2000\text{--}4000 \text{ m}$ , where a BPTL was observed. The trace  
295 gases such as ACE, ACN, and even  $\text{O}_3$  (Fig. 6b) have consistent peak times in the BPTL  
296 with concentrations of 3.0 ppb, 0.6 ppb, and 79 ppb, respectively. In this flight,  $\text{SO}_4^{2-}$

297 had the second-highest concentration among the aerosol components ( $1\text{--}2.4\ \mu\text{g m}^{-3}$ ;  
298 Figs. 6b and 6c) upstream of Taiwan ( $25\text{--}27\ ^\circ\text{N}$ ) during 1:00–3:00 UTC.

299 In the northern part of the flight between 03:00 and 05:00 UTC at an elevation of  
300  $>3000\ \text{m}$ , the aerosol component concentrations were all at their lowest level (Figs. 6b–  
301 6d). During 05:00–07:00 UTC, the HALO aircraft flew back southward to  $25\ ^\circ\text{N}$ , where  
302 high OA mass concentrations appeared again between 2000 and 4000 m (Figs. 6a, 6b,  
303 and 6d). Sulfate was the species with the highest concentration between 05:30 and  
304 06:30 UTC (Figs. 6b and 6c) when the flight's elevation was  $<1000\ \text{m}$  in the lower  
305 boundary between  $25$  and  $27\ ^\circ\text{N}$  (upstream of Taiwan). The reason explaining this  
306 observation is that the transport of anthropogenic pollutants of continental origin takes  
307 place mainly in the boundary layer (Figs. 6b–6d). Other aerosol species, such as  $\text{NO}_3^-$   
308 and  $\text{NH}_4^+$ , demonstrated low concentrations, except when the elevation was  $<1000\ \text{m}$ ,  
309 where they ranged up to  $1\ \mu\text{g m}^{-3}$  (Fig. 6b).

310 The 96-h HYSPLIT backward trajectory starting from the flight locations at  
311 02:00–07:00 UTC (Fig. 6e) indicated that the air masses at elevations between 2000  
312 and 4000 m were potentially transported from Indochina. North of  $30\ ^\circ\text{N}$  and at altitudes  
313 of  $>3000\ \text{m}$  at 04:00 UTC, the concentrations of air pollutants (including OA,  $\text{SO}_4^{2-}$ ,  
314  $\text{NO}_3^-$ , and  $\text{NH}_4^+$ ) were low (Figs. 6b and 6e) even though the air mass in the low  
315 boundary was sourced from SC and the Taiwan Strait. **In general, the BPTL was mainly**  
316 **located south of  $30\ ^\circ\text{N}$  as presented by Carmichael et al. (2003), and Tang et al. (2003).**  
317 **However, the ACN still could be around 300ppt or less as the flight at the north of  $30\ ^\circ\text{N}$**   
318 **(during 3:30–4:30 UTC) and could be recognized as the contribution of BB (Förster et al.**  
319 **2022). In other words, it might still have BB products being transported to the north of  $30$**   
320 **N under favorable weather conditions although the ACN concentration was low compared**  
321 **to the south of it at the layer of BPTL(between 2000 and 4000 m). The fact that higher**  
322 OA was observed rather in the higher altitudes than in the lower boundary also

323 demonstrated the vertical distribution over the ECS.

324 Figure 7 displays the vertical distribution of the gases and major aerosol  
325 components found on the flights on 17 (blue) and 19 (green) March 2018 as well as the  
326 mean concentrations noted in the seven flights (on 17, 19, 22, 24, 26, and 30 March and  
327 4 April 2018; red) to the ECS during EMERGe-Asia. Figure 7 illustrates all profiles  
328 calculated as 1-min mean and every 500-m interval with one standard deviation ( $\pm\sigma$ ).  
329 The number of the data points is displayed on the right side of each figure. The mean  
330 CO concentration profile demonstrated a decreasing trend from 240 ppb near the  
331 ground to 150 ppb at an altitude of 2500 m and 140–160 ppb at altitudes >6000 m (Fig.  
332 7a). The concentration for 17 March 2018 (flight F0317) was similar to the mean  
333 concentration profile, except for that at the <1500 m elevation in the lower boundary.  
334 However, a higher CO concentration (40–80 ppb) enhancement was noted on 19 March  
335 2018 (flight F0319) than the mean profile and flight F0317. The mean difference in CO  
336 concentration between flights F0319 and F0317 was as high as 80 ppb at an elevation  
337 of 3000–3500 m (Fig. 7a). Similarly, OA concentration was significantly higher in the  
338 BPTL vertical distribution in flight F0319 than in the mean profile and flight F0317  
339 (Fig. 7b). The mean OA concentration for the flight F0319 peaked at an elevation of  
340 2000–2500 m, increasing to  $2 \mu\text{g m}^{-3}$  more than in the mean profile and flight F0317.  
341 Other aerosol components such as  $\text{SO}_4^{2-}$ ,  $\text{NH}_4^+$ , and  $\text{NO}_3^-$  (Supplementary Fig. S2a-c)  
342 also had a similar vertical distribution trend, but the concentration differences were  
343 minor compared with OA concentrations. The magnitude of the maximum differences  
344 between the flights F0319 and F0317 in the BPTL was 1.3, 0.7, and  $0.4 \mu\text{g m}^{-3}$  for  
345  $\text{SO}_4^{2-}$ ,  $\text{NH}_4^+$ , and  $\text{NO}_3^-$ , respectively. The maximum difference concentration of BC can  
346 be as high as  $1.2 \mu\text{g m}^{-3}$  at 2000–2500 m between the flights F0319 and F0317 (Fig.7c).  
347 **Regarding the variations in ACN (Fig. 7d) and ACE ( Fig. 7e) in the BPTL, their**  
348 maximum mean concentrations in the flight F0319 were higher than those in the profile

349 of the flight F0317 by 0.18 and 0.9 ppb, respectively. In other words, flight F0319 had  
350 a more significant impact on the CO, OA, BC, and volatile organic compound (VOC)  
351 species such as ACN and ACE in the BPTL, which might account for the effect of BB  
352 emission transport from Indochina. The ozone concentration was lower in both flights  
353 F0317 and F0319 than in the mean profile at the elevations <2000 m (Fig. 7f). The  
354 ozone titration by NO<sub>x</sub> in the low boundary might also play a role. However, it was  
355 approximately 5–7 ppb higher in the flight F0319 than in the flight F0317 between the  
356 elevations of 1500 and 3000 m. In their downwind area, LRT of BB emissions might  
357 increase this concentration further at the BPTL (Tang et al., 2003; Lin et al., 2014) and  
358 also discussed in section 4. By contrast, the J value [J(O<sup>1</sup>D)] (Fig. 7g) was higher for  
359 flight F0317 than for F0319 in the elevation range 1000–3000 m, in line with high aerosol  
360 concentrations and associated cloud enhancement that typically lead to decreased  
361 photolysis frequencies [i.e., J(O<sup>1</sup>D)] (Tang et al., 2003). Figure S3 (Supplementary)  
362 indicated the aircraft measurement for the J value (J(O<sup>1</sup>D)) and CCN (Cloud  
363 Condensation Nuclei; at a constant instrument supersaturation of 0.38 %) along the  
364 flight on 19 March 2018. The CCN number concentration (per cm<sup>3</sup>), was consistently  
365 increased with the aerosol species (such as OA) as the flight passed through the BPTL  
366 (2000-4000 m). Consistently, at altitudes >4000 m the presence of clouds below the aircraft  
367 led to greater J values.

368 The concentrations of other species such as NO<sub>y</sub> (Fig.7h) and HONO  
369 (Supplementary Fig. S2d) were also greater in flight F0317 than in flight F0319 by 0.4-  
370 1.2 ppb and 10-34 ppt, respectively, in the low boundary (<1500 m). At the BPTL, the  
371 concentration of NO<sub>y</sub> (1-2 ppb) in the flight F0319 was higher than in the flight F0317,  
372 but the difference was less than 0.6 ppb. The results from the TRACE-P campaign,  
373 which examined the Asian outflow of NO<sub>y</sub>, also demonstrated large increases in NO<sub>y</sub>  
374 concentrations (0.5-1 ppb) downwind from Asia. The NO<sub>y</sub> consisted mainly of HNO<sub>3</sub>

375 and peroxyacetyl nitrate (Miyazaki et al., 2003; Talbot et al., 2003).

376

## 377 **4 Simulation results and discussion**

### 378 **4.1 Model performance and BB transport identification**

379 Tables 2 and 3 and Fig. 8 plot the Pearson correlation coefficients between 5-min  
380 merged observations on board the HALO and the simulation for flights F0317 and  
381 F0319. Meteorological parameters such as potential temperature ( $\theta$ ), relative  
382 humidity (RH), and wind speed (WS) were all captured well by the model along the  
383 HALO flight path on the 2 days. The correlation coefficient (R) for meteorological  
384 parameters was high, ranging from 0.92 to 0.99 (Table 2). The strong correlation  
385 indicates the high representativeness of the reanalysis of meteorological data used in  
386 the simulation. Among the trace species and aerosol components, toluene (TOL),  $\text{NO}_x$ ,  
387 BC, OA, ketones (KET), HONO,  $\text{SO}_2$ , and HCHO demonstrated an R of  $>0.5$  (good  
388 correlation) and CO and  $\text{O}_3$  showed an R of nearly 0.5 (Table 2). The simulation  
389 performance was investigated in the BL ( $<1000$  m; Fig. 8), at 2000–4000 m altitude  
390 (Table 3 and Fig. 8) and for the whole period of both flights (Table 2 and Fig. 8; blue  
391 dot). Even in the BPTL, the simulated meteorological parameters presented a good  
392 correlation ( $R > 0.93$ ), followed by OA, BC, KET, CO,  $\text{O}_3$ ,  $\text{NO}_x$  as well as  $\text{NH}_4^+$  and  
393  $\text{NO}_y$  ( $R > 0.5$ ) (Table 3). In other words, at the BPTL, the R for the simulation  
394 significantly increased for OA, BC, CO,  $\text{O}_3$ ,  $\text{NO}_y$  and KET (Tables 2 and 3 and Fig. 8),  
395 which are indicators for BB being a source of pollution in the model. In contrast,  $\text{SO}_4^{2-}$ ,  
396  $\text{NO}_3^-$ ,  $\text{SO}_2$ ,  $\text{NO}_x$ , TOL, XYL, HCHO and HONO had better correlation in the lower part  
397 of the boundary layer, at altitudes  $<1000$  m (see Fig. 8) than in the BPTL. We explain  
398 this by the transport of anthropogenic pollutants in the continental outflow in the lower  
399 part of the boundary layer in ECS.

400 The modeling results tended to overestimate the concentration of the species, with

401 examples being CO (64 ppb), OA ( $0.3 \mu\text{g m}^{-3}$ ), BC ( $0.2 \mu\text{g m}^{-3}$ ) and O<sub>3</sub> (12.5 ppb;  
402 Table 3) in the BPTL. Because high concentrations of CO, BC and OA in BPTL are  
403 accurate indicators of BB in the model, the BB emission from the source of FINN data  
404 are probably also overestimated (Lin et al., 2014). Except for OA and BC, the  
405 correlations for other aerosol components such as NO<sub>3</sub><sup>-</sup>, and SO<sub>4</sub><sup>2-</sup> were poor (0.13 and  
406 0.2, respectively). The poor correlation for SO<sub>4</sub><sup>2-</sup> may result from the large uncertainty  
407 in the emission of SO<sub>2</sub>.

408 Because the meteorological parameters were simulated well, the simulation  
409 discrepancies for chemical species are either caused by the emission estimation  
410 uncertainties or by inaccuracies in the simulation of chemical oxidation processes  
411 during LRT. Because CO, OA, and BC are accurate indicators of simulated BB  
412 transport from Indochina (Carmical et al., 2003), the airborne measurements on board  
413 the HALO are used as reference to evaluate the performance of the model for the flight  
414 F0319 (Fig. 9). The 5-min merged simulation of CO concentration with (blue line) and  
415 without (green line) BB was compared to that measured on board the HALO (red line);  
416 the concentration was mostly in the range of 100–200 ppb, with its peak approaching  
417 300 ppb (at 01:50, 02:50, and 04:00 UTC) at the BPTL (Fig. 9a). In general, the  
418 simulation captured the CO variation along the flight path. However, it overestimated  
419 the observations by nearly 100 ppb for the simulation with BB at the BPTL during  
420 01:00–02:00, 03:40–04:20, 05:00–05:40, and 06:30–07:20 UTC (Fig. 9a). Notably, the  
421 simulation difference was minor when the flight was in the lower part of the boundary  
422 layer (02:30 and 06:00 UTC) i.e. < 1000m or at elevations of >4000 m (03:00–03:30  
423 and 04:20–05:00 UTC). The model underestimated CO concentration in the lower part  
424 of the boundary (<1000 m) (02:30 and 05:50–06:30 UTC) over the ECS. In conclusion,  
425 our model simulation overestimates BB emissions but underestimates continental CO  
426 emissions from China due to the underestimation of the emission inventory of the



427 MICS-Asia III (Kong et al.,2020) was adopted in this study.

428 OA and BC are also important BB indicators and were reasonably captured by the

429 model before 03:00 UTC when the flight was south of 28 °N at elevations of <4000 m

430 (Fig. 9 b-c). The time series of simulated OA and BC has peak concentrations of nearly

431  $4\text{--}5.5\ \mu\text{g m}^{-3}$  and  $2\ \mu\text{g m}^{-3}$ , respectively, during HALO shuttle flights passing through

432 the BPTL (2000–4000 m) around 01:50 and 02:50 UTC. When BB emission was not

433 included in the simulation, the concentration peaks were not observed (see Fig. 9b-c,

434 green plot). Similar to the simulated CO results, the simulated OA and BC overestimate

435 the amounts of these species to the north of 28 °N during 03:30-04:20 UTC (Fig. 6a

436 and 9). Furthermore, when the simulation only considered direct effect (case ROCD,

437 purple), the overestimations were increased as shown in Figure 9b-c. As mentioned

438 earlier, a frontal system was just located from the ECS to SC (Fig. 2e) on 19 March

439 2018. In other words, the effect of wet scavenging reduced the aerosol concentration

440 bias in the ECS and SC, as for the frontal system providing the moist air mass in the

441 event flight F0319. The model after 07:30 UTC, which was related to local emissions

442 before HALO landed over western Taiwan on 19 March 2018. In general, our model

443 simulation captured reasonably well OA and BC with an R of 0.61 and 0.74,

444 respectively. A minor mean bias for OA (BC) is  $0.3\ \mu\text{g m}^{-3}$  ( $0.1\ \mu\text{g m}^{-3}$ ) and the root

445 mean square error (RMSE) of OA (BC) is  $1.1\ \mu\text{g m}^{-3}$  ( $0.4\ \mu\text{g m}^{-3}$ ) (Table 2). The R for

446 OA (BC) reached 0.85(0.79), with an RMSE of  $0.7 \mu\text{g m}^{-3}$  ( $0.5 \mu\text{g m}^{-3}$ ) when we  
447 calculated the BB transport layer only between 2000 and 4000 m (Table 3 and Fig. 8).  
448 In addition to OA and BC, simulated aerosol species such as  $\text{SO}_4^{2-}$  was overestimated,  
449 whereas  $\text{NO}_3^-$  was underestimated although their concentrations were low (Table 3).  
450 Because the BPTL was mainly between altitudes of 2000 and 4000 m, the subsequent  
451 discussion focuses on the influence of the BPTL from Indochina on the downstream  
452 areas, particularly the ECS and Taiwan.

#### 453 **4.2 Effects of LRT BB plume from Indochina on East Asia**

454 To investigate the regional impacts of BB plume transport from Indochina, we  
455 compared the simulation with and without BB emission for the events on 17 and 19  
456 March 2018. The analysis of the calculations focused on the impact over SC, Taiwan  
457 and ECS. These three selected regions are SCA (in South China), TWA (covered the  
458 whole Taiwan), and ECSA (in the ECS) as shown in Figure 1a. After being emitted the  
459 BB pollutants from Indochina were then transported northward to China and  
460 subsequently northeastward. The exact flow pattern depended on the weather  
461 conditions and flow types (ridge or trough) at 700 hPa (3000 m) between 17 and 19  
462 March 2018 (see Fig. 2). Consequently, we investigated the hourly variation in the area  
463 mean concentrations or mixing ratios of air pollutant trace constituents to assess the  
464 importance of BB emissions from Indochina on the selected downstream region e.g. the  
465 ECSA (Fig. 10), SCA, TWA and ECSA (Table 4). The contribution of CO (or others  
466 species) due to BB was estimated by the difference between simulations with and  
467 without the BB emission. These differences are then expressed as a fraction in  
468 percentage shown in Figure 10 (blue line). The mean concentration of CO (red line)

469 over the ECSA (Fig. 10a) was at its lowest (115 ppb) on 17 March 2018; it gradually  
470 increased to a peak concentration of 280 ppb on 18 March 2018 and then remained  
471 stable at 260 ppb on 19 March 2018. The contribution of CO from BB (blue line)  
472 ranged from 19 % (<22 ppb) on 17 March 2018 to a peak of 42 % (~113 ppb) on 18  
473 March 2018 and then gradually declined to 26 % on 19 March 2018 (Fig. 10a). As  
474 for OA (BC), the lowest percent contribution by BB was 14-16% (<5%) between 16  
475 and 17 March 2018 while the highest could be more than 40% (80%) during 18 and 19  
476 March 2018 (Fig. 10b and c). The BB contributed to PM<sub>2.5</sub> was 19 % (0.39  $\mu\text{g m}^{-3}$ ) on  
477 17 March 2018 (Fig. 10d), increasing to 45 % (3.6  $\mu\text{g m}^{-3}$ ) on 18-19 March 2018  
478 because the BB plume spread by the strong wind to the ECSA.

479 The variation of O<sub>3</sub> (Fig. 10e) depends on transport and photochemistry, which  
480 involves the precursors NO<sub>x</sub> and VOC and the photolysis frequency of NO<sub>2</sub>, J(NO<sub>2</sub>).  
481 For the elevations between 2000–4000 m, O<sub>3</sub> changes are similar to those of CO, NO<sub>x</sub>  
482 and KET, which were mainly contributed by the LRT BB plume and related to the  
483 ozone precursor after 18 March 2018. The lowest and highest O<sub>3</sub> concentrations on 17  
484 and 18 March 2018 were 56 and 75 ppb, respectively, of which we estimate that 5.6  
485 ppb (10 %) and 34 ppb (45 %) were BB's contributions, respectively. Although the  
486 mean NO<sub>x</sub> concentration was relatively small (0.06–0.18 ppb), the BB contributed 35–  
487 70 % (0.02–0.13 ppb) during 17–19 March 2018 (Supplementary Fig. S4a). The KET  
488 concentration was in the range 0.4 to 2.7 ppb, with BB contributing nearly 20–26 %  
489 (0.08–0.7 ppb) during 17–19 March 2018 (Supplementary Fig. S4b).

490 The area-mean OH contributed by BB increased from its lowest level (<30 %) on  
491 17 March 2018 to its highest (nearly 70 %) on 19 March 2018 (Fig. 10f). HO<sub>2</sub> was also  
492 observed to increase trend from 10 % to 40 % during daytime over the period 17–19  
493 March 2018 (Supplementary Fig. S4c). The amounts of the oxidizing agent, OH, and  
494 the free radical HO<sub>2</sub> depend on the amounts of trace gases, which produce and remove

495 these radicals, (eg.  $\text{NO}_x$ , water vapor, ozone, hydrocarbons, etc.) and the relevant  
496 photolysis frequencies  $J(\text{O}_3 \rightarrow \text{O}^1\text{D})$ ,  $J(\text{NO}_2)$  etc.. Thus trace constituents from BB were  
497 expected to increase OH and  $\text{HO}_2$ . However, BB's contribution to photolysis  
498 frequencies  $J(\text{O}_3 \rightarrow \text{O}^1\text{D})$  (Fig. 10g),  $J(\text{NO}_2)$  (Supplementary Fig. S4d) etc. decreased  
499 as the mean BB aerosol concentration increased over the ECS during 17–19 March  
500 2018. This is because photolysis calculation results used simulated aerosol and cloud  
501 formation, which increased over the ECSA (Fig. 12).

502 The  $\text{NO}_y$ , mean concentration ranged from 1.0 to 4.5 ppb, of which BB's  
503 contribution was from 55 to 82 % (Supplementary Fig. S4e). Such a high contribution  
504 from BB also demonstrated the effects of long-distance transport. Figure 10h indicates  
505 an increasing trend of HCHO concentration from 17 to 19 March 2018. HCHO  
506 formation and destruction depend on the rate of reaction of OH with HCHO precursors  
507 and the rate of reaction of HCHO with OH and the photolysis frequency of HCHO. As  
508 a result, HCHO production varied with OH concentration. The lowest and highest  
509 concentrations of HCHO were on 17 and 19 March 2018, respectively. In summary,  
510 the consistent variations in BB contributions to CO, OA, BC,  $\text{PM}_{2.5}$ , OH, HCHO,  $\text{NO}_x$ ,  
511  $\text{NO}_y$ , and  $\text{O}_3$  peaked on 18 or 19 March 2018, whereas  $J(\text{O}^1\text{D})$  decreased between 17  
512 and 19 March 2018.

513 Figure 11 displays the fraction in % that the long-range transported BB emission  
514 contributes to the amounts of  $\text{NO}_x$ ,  $\text{NO}_y$ ,  $\text{PM}_{2.5}$ , OA, BC, OH,  $\text{O}_3$ , CO, KET,  $\text{HO}_2$ ,  
515 HCHO and  $J(\text{O}^1\text{D})$ , over the ECSA on 17 and 19 March 2018. Except for  $\text{NO}_y$ , BB  
516 contribution was generally <11 % at elevations of <1000 m over the ECSA. The scatter  
517 distribution of the simulation results indicates that the effect of BB emission at  
518 elevations of <1000 m (Fig. 11a) was significantly lower than that between the  
519 elevations of 2000 and 4000 m (Fig. 11b). For  $\text{NO}_y$ ,  $\text{NO}_x$ ,  $\text{PM}_{2.5}$ , BC, OH,  $\text{O}_3$ , and CO,  
520 the BB contribution was >30 % at the elevation of 2000–4000 m over the ECSA (Fig.

521 11b). Table 4 further summarizes the effect of BB emission on the downwind areas  
522 (SCA, TWA, and the ECSA) at the <1000 m and 2000–4000 m elevations. The  
523 contribution of BB to NO<sub>y</sub>, NO<sub>x</sub>, PM<sub>2.5</sub>, BC, OH, O<sub>3</sub> and CO was at least 30–80 % at  
524 the elevation of 2000–4000 m over the regions SCA, TWA and ECSA (Table 4). In the  
525 lower boundary layer (i.e. <1000 m), the BB contribution for most species at the remote  
526 downstream areas was <20 %, except for TWA. Because of the high mountains (Lin et  
527 al. 2021) present in TWA, the BB plume passing over Taiwan was potentially  
528 transported downward through mountain–valley circulation to the lower boundary layer  
529 (Ooi et al., 2021). The influence of BB over TWA was the highest among these three  
530 downstream regions (see Table 4) as its location was directly on the transport pathway  
531 for the BB plume on the major event day (flight F0319).

532 Figure 12a displays the simulated cloud water difference with and without BB  
533 emission over different regions on 17 and 19 March 2018. BB aerosols are a potential  
534 source of cloud nuclei. The simulations show the impact of BB on cloud water  
535 enhancement (Fig. 12a) in the vertical distribution. Cloud water enhancement over SCA  
536 was associated with aerosol enhancement from the BB in the altitude range 1000–4000  
537 m: the peak being 1.8–2.0 mg kg<sup>-1</sup> at 2000 m on these 2 days (Fig. 12a). The abundance  
538 of BB emissions transported from Indochina to SCA (Fig. 3) is expected to contribute  
539 to the high cloud water formation over SCA. Furthermore, the southerly flow (Fig. 3)  
540 that transports warm and moist air mass from the South China Sea may have favored  
541 cloud formation in flights F0317 and F0319. High cloud water related to BB can be  
542 seen in the simulations of these two days. In the remote ECSA regions, the cloud water  
543 substantially increased on 19 March 2018 (Fig. 12a) compared to 17 March 2018  
544 because of a significant difference in BB emissions transported to the ECSA between  
545 17 and 19 March 2018 (Fig. 3). Similarly, the cloud water enhancement over Taiwan  
546 also only appeared on 19 March 2018 (Fig. 12a). Furthermore, nearly no difference in

547 the cloud water vertical distribution over the region IDCA (Fig. 1a) in Indochina was  
548 noted because in the Indochina region, spring is the dry season (Lin et al., 2009) and  
549 thus unfavorable for cloud water formation. Figure 12b shows the cloud water  
550 difference when the aerosol indirect effect turned off in the simulation over different  
551 regions on 19 March 2018. The significant cloud water shortage over ECSA, and SCA  
552 could be as high as 2.4 mg/kg and 1.5 mg/kg, respectively (Fig.12b). In other words,  
553 the role of the chemistry-microphysics interactions (indirect effect) plays an important  
554 role in the cloud water enhancement in the SCA and ECSA in this study.

555 The simulated downward shortwave flux at the noontime at ground surface due  
556 to BB was 2-4% and 5-7% reduction over the regions ECSA and SCA, respectively,  
557 (supplementary Fig. S5a-b, blue line) during 18-19 March 2018. However, a significant  
558 shortwave flux reduction at the noontime at ground surface could be 15-20% due to  
559 aerosol indirect effect in the region SCA during 18-19 March 2018 (supplementary Fig.  
560 S5a-b blue dashed line). The combination of BB aerosols enhancement and increased  
561 cloud water results in shortwave radiation reduction, implying the possibility of  
562 regional climate change in East Asia driven by BB aerosols.

563

## 564 **5. Summary**

565 The BB during spring in Indochina has a significant impact on the chemistry and  
566 composition of the troposphere in the surrounding regions of East Asia. During the  
567 EMeRGe campaign in Asia, atmospheric pollutants were measured on board the HALO  
568 aircraft. In this study, a minor long-range BB transport event was observed from  
569 Indochina on 17 March 2018 (flight F0317), followed by a major long-range BB  
570 transport event on 19 March 2018 (flight F0319). The impact on tropospheric trace  
571 constituent composition and the environment has been investigated.

572 During the major BB transport event F0319, the 1-min mean of the peak

573 concentrations of the trace constituents CO, O<sub>3</sub>, ACE, ACN, OA and BC between the  
574 altitudes of 2000 and 4000 m over the ECS were 312.0 ppb, 79.0 ppb, 3.0 ppb, 0.6 ppb,  
575 6.4  $\mu\text{g m}^{-3}$ , 2.5  $\mu\text{g m}^{-3}$  respectively. In comparison during the F0317 event CO, O<sub>3</sub>,  
576 ACE, ACN, OA and BC were 203.0 ppb, 71.0 ppb, 2.0 ppb, 0.3 ppb, 3.4  $\mu\text{g m}^{-3}$ , 1.2  
577  $\mu\text{g m}^{-3}$  respectively.

578 When the elevation was <1000 m for both the F0317 and F0319 events, the sulfates,  
579 rather than OA, had the highest concentrations. The peak concentration could be as high  
580 as 5.1  $\mu\text{g m}^{-3}$  in the low boundary for the event F0317 in the ECS. This observation is  
581 most likely explained by a continental outflow from regions having fossil fuel  
582 combustion in the lower boundary layer over the ECS.

583 In this study, the WRF-Chem model was employed to evaluate the BB plume  
584 transported from Indochina and its influence on the downstream areas including South  
585 China, Taiwan, and the ECS. The contribution of the BB plume for most species in the  
586 remote downstream areas was <20 % in the lower boundary layer (altitude <1000 m).  
587 In comparison, the contribution of long-range transported BB plume was 30–80 %, or  
588 even higher, for many of the trace constituents (NO<sub>y</sub>, NO<sub>x</sub>, CO, OH, O<sub>3</sub>, BC and PM<sub>2.5</sub>)  
589 in the altitude range between 2000 and 4000 m for SC, Taiwan, and the ECS. The large  
590 influence of BB over Taiwan is most probably because the BB transport passes directly  
591 over Taiwan.

592 BB aerosols are potential sources of cloud nuclei. The WRF simulations estimate  
593 the effect of the BB plume on cloud water formation over SC and the ECS. We observe  
594 in the simulations cloud water enhancement over SC at elevations of 1000–4000 m.  
595 This increase of cloud water is consistent with an increase in aerosol, caused by BB  
596 emissions, transported from Indochina to SC. In remote regions of the ECS, the  
597 simulated cloud water was significantly larger during the major BB event on 19 March  
598 2018 than the minor BB event on 17 March 2018. The simulated decrease of the

599 photolysis frequency ( $J(\text{O}^1\text{D})$  and  $J(\text{NO}_2)$ ) is attributed to the difference in aerosol  
600 concentrations and associated cloud enhancement between the two events over the ECS.  
601 This we explain by the significant differences in BB emissions transported to the ECS  
602 between the two events. **The combination of increased BB aerosol concentration and**  
603 **increased amounts of cloud water led to reductions in the amount of incoming**  
604 **shortwave radiation at the surface over the ECS and SC. This influences tropospheric**  
605 **chemistry and composition, regional climate, precipitation, ocean biogeochemistry,**  
606 **agriculture, and human health.**

607

#### 608 ***Data availability***

609 The EMERGe data are available at the HALO database  
610 (<https://doi.org/10.17616/R39Q0T>, DLR, 2022) and can be accessed upon registration.  
611 Modeling data can be made available upon request to the corresponding author.

#### 612 ***Author contribution***

613 CYL conceived the idea, analyzed the data, writing and editing of the manuscript. WNC  
614 and YYC run the model and analyzed the data. CKC joined the manuscript  
615 discussion. CYLiu provided the MODIS data. HZ and HS provided trace gases data. EF  
616 provided acetonitrile data. FO performed the ozone measurement. OOK, BAH and  
617 MLP were responsible for the BC measurement. KK and JS were responsible for C-  
618 ToF-MS measurements. KP and BW provided HONO data. JPB and MDAH led the  
619 EMERGe-Asia experiment. All authors have read and agree to the published version of  
620 the manuscript.

#### 621 ***Competing interests***

622 The authors declare that they have no conflict of interest.

#### 623 ***Acknowledgments:***

624 The accomplishment of this work has financial support from the Ministry of Science  
625 and Technology, Taiwan, under grants MOST 108-2111-M-001-002, 109-2111-M-001-  
626 004 and 110-2111-M-001-013. We thank to National Center for High-performance  
627 Computing (NCHC) for providing computational and storage resources.

628 The HALO deployment during EMERGe was funded by a consortium comprising the  
629 German Research Foundation (DFG) Priority Program HALO-SPP 1294, the Institute  
630 of Atmospheric Physics of DLR, the Max Planck Society (MPG), and the Helmholtz



631 Association. Johannes Schneider and Katharina Kaiser acknowledge funding through  
632 the DFG (project no. 316589531).

633 **References:**

634 Ackermann, I. J., Hass, H., Memmsheimer, M., Ebel, A., Binkowski, F. S., and Shankar,  
635 U.: Modal aerosol dynamics model for Europe: development and first applications,  
636 *Atmos. Environ.*, 32, 2981–2999, [https://doi.org/10.1016/S1352-2310\(98\)00006-5](https://doi.org/10.1016/S1352-2310(98)00006-5),  
637 1998.

638 Ahmadov, R., McKeen, S. A., Robinson, A. L., Bahreini, R., Middlebrook, A. M., de  
639 Gouw, J. A., Meagher, J., Hsie, E.- Y. Edgerton, E., Shaw, S., and Trainer, M.: A  
640 volatility basis set model for summertime secondary organic aerosols over the  
641 eastern United States in 2006, *J. Geophys. Res.*, 117,  
642 <https://doi.org/10.1029/2011JD016831>, 2012.

643 Andrés Hernández, M. D., Hilboll, A., Ziereis, H., Förster, E., Krüger, O. O., Kaiser,  
644 K., Schneider, J., Barnaba, F., Vrekoussis, M., Schmidt, J., Huntrieser, H.,  
645 Blechschmidt, A.-M., George, M., Nenakhov, V., Harlass, T., Holanda, B. A., Wolf,  
646 J., Eirenschmalz, L., Krebsbach, M., Pöhlker, M. L., Kalisz Hedegaard, A. B., Mei,  
647 L., Pfeilsticker, K., Liu, Y., Koppmann, R., Schlager, H., Bohn, B., Schumann, U.,  
648 Richter, A., Schreiner, B., Sauer, D., Baumann, R., Mertens, M., Jöckel, P., Kilian,  
649 M., Stratmann, G., Pöhlker, C., Campanelli, M., Pandolfi, M., Sicard, M., Gómez-  
650 Amo, J. L., Pujadas, M., Bigge, K., Kluge, F., 770 Schwarz, A., Daskalakis, N.,  
651 Walter, D., Zahn, A., Pöschl, U., Bönisch, H., Borrmann, S., Platt, U. and Burrows,  
652 J. P.: Overview: On the transport and transformation of pollutants in the outflow of  
653 major population centres –observational data from the EMeRGe European intensive  
654 operational period in summer 2017. *Atmos. Chem. Phys.*, 22, 5877–5924,  
655 <https://doi.org/10.5194/acp-22-5877-2022>, 2022.

656 Carmichael, G. R., Tang, Y., Kurata, G., Uno, I., Streets, D., Woo, J.-H., Huang, H.,  
657 Yienger, J., Lefer, B., Shetter R. et al.: Regional-scale chemical transport modeling  
658 in support of the analysis of observations obtained during the TRACE-P experiment,  
659 *J. Geophys. Res.*, 108(D21), 8823, doi:10.1029/ 2002JD003117, 2003.

660 Chuang, M.T., Fu, J.S., Lee, C.T., Lin, N.H., Gao, Y., Wang, S.H., Sheu, G.R., Hsiao,  
661 T.C., Wang, J.L., Yen, M.C., Lin, T.H. and Thongboonchoo, N.: The simulation of  
662 long-range transport of biomass burning plume and short-range transport of  
663 anthropogenic pollutants to a mountain observatory in East Asia during the 7-  
664 SEAS/2010 Dongsha Experiment. *Aerosol Air Qual. Res.* 16: 2933–2949, 2016.

665 Chi K H., C. Y. Lin, C.F.Ouyang, J.Lin Lin, N.H. Lin, G.R. Sheu, C. T. Lee: PCDD/F  
666 Measurement at a High-altitude Station in Central Taiwan: Evaluation of Long-range  
667 Transport of PCDD/Fs during the Southeast Asia Biomass Burning Event,

668 *Environmental Science & Technology*,44,2954-2960, DOI: 10.1021/es1000984  
669 <https://doi.org/10.1021/es1000984>, 2010.

670 Ding K., Huang X., Ding A., Wang M., Su H., et al.: Aerosol-boundary-layer-monsoon  
671 interactions amplify semi-direct effect of biomass smoke on low cloud formation in  
672 Southeast Asia., *Nature Communications*, 12:6416, 2021.

673 Förster, E., Bönisch, H., Neumaier, M., Obersteiner, F., Zahn, A., Hilboll, A., Kalisz  
674 Hedegaard, A. B., Daskalakis, N., Poulidis, A. P., Vrekoussis, M., Lichtenstern, M.,  
675 and Braesicke, P.: Chemical and dynamical identification of emission outflows  
676 during the HALO campaign EMeRGe in Europe and Asia, *Atmos. Chem. Phys.*  
677 *Discuss. [preprint]*, <https://doi.org/10.5194/acp-2022-455>, in review, 2022.

678 Fu, J. S., Hsu, N. C., Gao, Y., Huang, K., Li, C., Lin, N.-H., and Tsay, S.-C.: Evaluating  
679 the influences of biomass burning during 2006 BASE-ASIA: a regional chemical  
680 transport modeling, *Atmos. Chem. Phys.*, 12, 3837–3855,  
681 <https://doi.org/10.5194/acp-12-3837-2012>, 2012.

682 Galanter, M., Levy, H., Carmichael, G. R.: Impacts of biomass burning on tropospheric  
683 CO, NO<sub>x</sub>, and O<sub>3</sub>, *J. Geophys. Res. Atmos.*, 105, 6633-6653, 2000.

684 Giglio, L., Randerson, J.T., Werf, G.R.V.D.: Analysis of daily, monthly, and annual  
685 burned area using the fourth-generation global fire emissions database (GFED4). *J.*  
686 *Geophys. Res. Biogeosci.* 118 (1), 317–328., 2013.

687 Grell, G. A., Peckham, S. E., Schmitz, R., McKeen, S. A., Frost, G., Skamarock, W. C.,  
688 and Eder, B.: Fully coupled “online” chemistry within the WRF model, *Atmos.*  
689 *Environ.*, 39, 6957–6975, <https://doi.org/10.1016/j.atmosenv.2005.04.027>, 2005.

690 Heald, C. L., Jacob D.J., Fiore, A.M., Emmons, L. K., et al.: Asian outflow and trans-  
691 Pacific transport of carbon monoxide and ozone pollution: An integrated satellite,  
692 aircraft, and model perspective, *J. Geophys. Res.*, 108(D24), 4804,  
693 doi:10.1029/2003JD003507, 2003.

694 Hong, S., Lakshmi V., Small, E.E., Chen, F., Tewari, M., Manning, K.W.: Effects of  
695 vegetation and soil moisture on the simulated land surface processes from the  
696 coupled WRF/Noah model. *J Geophys Res* 114(D18), D18118, 2009.

697 Huang, K., Fu, J. S., Hsu, N.C., Gao, Y., Dong, X., Tsay, S. C., Lam, Y. F.: Impact  
698 assessment of biomass burning on air quality in Southeast and East Asia during  
699 BASE-ASIA, *Atmospheric Environment*, 78, 291e302, 2013.

700 Jacob, D.J., Crawford, J. H. Kleb, M. M.,Connors, V. S, Bendura, R. J., Raper, J. L.,  
701 Sachse,G. W., Gille, J. C., Emmons, L., Heald, C. L.: The transport and chemical  
702 evolution over the pacific (trace-P) aircraft mission: design, execution, and first  
703 results. *J. Geophys. Res. Atmos.* 108 (D20), 2003.

704 Janjic, Z.I.: The step-mountain eta coordinate model: further developments of the  
705 convection,viscous layer, and turbulence closure schemes, *Mon.Wea. Rev.*, 122,

706 927–945, 1994.

707 Kong L., Tang X., Zhu J., Wang Z., Fu J.S., Wang X., et al.: Evaluation and uncertainty  
708 investigation of the NO<sub>2</sub>, CO and NH<sub>3</sub> modeling over China under the framework  
709 of MICS-Asia III. *Atmos. Chem. Phys.*, 20, 181–202, 2020.  
710 <https://doi.org/10.5194/acp-20-181-2020>

711 Li, J., Nagashima, T., Kong, L., Ge, B., Yamaji, K., Fu, J. S., Wang X., Fan, Q., Itahashi,  
712 S., et al.: Model evaluation and inter-comparison of surface-level ozone and relevant  
713 species in East Asia in the context of MICS-ASIA phase III Part I: overview. *Atmos.*  
714 *Chem. Phys.*, 19, 12993–13015, <https://doi.org/10.5194/acp-19-12993-2019>, 2019.

715 Lin, C.Y., Hsu, H.M., Lee, Y.H., Kuo, C. H., Sheng, Y.F., Chu, D. A.: A new transport  
716 mechanism of biomass burning from Indochina as identified by modeling studies.,  
717 *Atmos. Chem. Phys.*, 9, 7901-7911. <https://doi.org/10.5194/acp-9-7901-2009>, 2009.

718 Lin, C. Y., Chou, C.C.K, Wang, Z., Lung, S.C., Lee, C. T., Yuan, C.S., Chen, W. N.,  
719 Chang, S. Y., Hsu, S. C., Chen, W. C., Liu, Shaw. C.: Impact of different transport  
720 mechanisms of Asian dust and anthropogenic pollutants to Taiwan. *Atmospheric*  
721 *Environment*, 60,403-418, <http://dx.doi.org/10.1016/j.atmosenv.2012.06.049>, 2012.

722 Lin, C. Y., Zhao, Liu, C. X, Lin, N. H., Chen, W. N.: Modeling of long-range transport  
723 of Southeast Asia biomass burning pollutants to Taiwan and their radiative forcing  
724 over East Asia, *Tellus B*, 66, 1-17. 23733.  
725 <http://dx.doi.org/10.3402/tellusb.v66.23733>, 2014.

726 Lin, C.Y., Sheng, Y. F., Chen, W. C., Chou, C.C. K., Chien, Y. Y., Chen, W. M.: Air  
727 quality deterioration episode associated with typhoon over the complex topographic  
728 environment in central Taiwan. *Atmos. Chem. Phys.*, 21, 16839-16910.  
729 <https://doi.org/10.5194/acp-21-16893-2021>, 2021.

730 Lin, N.H., Tsay, S.C., Reid, J. S., Yen, M.C., Sheu, G. R., Wang, S.H., Chi, K.H., et al. :  
731 An overview of regional experiments on biomass burning aerosols and related  
732 pollutants in Southeast Asia: From BASE-ASIA and Dongsha Experiment to 7-  
733 SEAS. *Atmos. Environ.* 78: 1–19, 2012.

734 Marvin, M. R., Palmer P. I., Latter, B. G., Siddans, R., Kerridge, B.J., Latif, M. T., Khan,  
735 M. F.: Photochemical environment over Southeast Asia primed for hazardous ozone  
736 levels with influx of nitrogen oxides from seasonal biomass burning. *Atmos. Chem.*  
737 *Phys.*, 21, 1917–1935. <https://doi.org/10.5194/acp-21-1917-2021>, 2021.

738 Miyazaki Y., Kondo Y., Koike M., Fuelberg H. E., Kiley C. M., Kita K., Takegawa N.,  
739 Sachse G. W., Flocke F., Weinheimer A. J., Singh H. B., Eisele F. L., Zondlo M.,  
740 Talbot R. W., Sandholm S. T., Avery M. A., Blake D. R.: Synoptic-scale transport of  
741 reactive nitrogen over the western Pacific in spring, *J. Geophys. Res.*,  
742 108(D20),8788, doi:10.1029/2002JD003248., 2003.

743 Morrison H., Curry, J.A., Khvorostyanov, V.I.: A new double-moment microphysics

744 parameterization for application in cloud and climate model. PartI: Description.  
745 *Journal of the Atmospheric Sciences.*, 62, 1665-1676, 2005.

746 Neu, J. L., and Prather, M. J.: Toward a more physical representation of precipitation  
747 scavenging in global chemistry models: Cloud overlap and ice physics and their  
748 impact on tropospheric ozone. *Atmo. Chem. and Phys.*, 12, 3289–3310.  
749 <https://doi.org/10.5194/acp-12-3289-2012> ,2012

750 Palmer, P. I., Jacob, D. J., Jones, D. B. A., Heald, C. L., Yantosca, R. M., Logan, J. A.,  
751 Sachse, G. W. and Streets, D. G.: Inverting for emissions of carbon monoxide from  
752 Asia using aircraft observations over the western Pacific, *J. Geophys. Res.*, 108(D21),  
753 8828, doi:10.1029/2003JD003397, 2003.

754 Pimonsree, S., Vongruang, P., Sumitsawan, S.: Modified biomass burning emission in  
755 modeling system with fire radiative power: Simulation of particulate matter in  
756 Mainland Southeast Asia during smog episode. *Atmospheric Pollution Research*, 9,  
757 133-145. <http://dx.doi.org/10.1016/j.apr.2017.08.002>, 2018.

758 Powers G., J. B. Klemp, W. C. Skamarock, C. A. Davis, J. Dudhia, D. O. Gill, et al.The  
759 weather research and forecasting model Overview, System Efforts, and Future  
760 Directions. *Bulletin of the American Meteorological Society*, 98,1717-1737, 2017.

761 Ramanathan, V., Ramana, M. V., Roberts, G., Kim, D., Corrigan, C., Chung, C., and  
762 Winker, D.: Warming trends in Asia amplified by brown cloud solar absorption.  
763 *Nature*, 448, 575-U575, 2007.

764 Reid, J. S., Hyer, E. J., Johnson, R. S., Holben, B. N., Yokelson, R. J., Zhang, J., et al. :  
765 Observing and understanding the Southeast Asian aerosol system by remote sensing:  
766 An initial review and analysis for the Seven Southeast Asian Studies (7SEAS)  
767 program, *Atmospheric Research*, 122, 403-468, 2013.

768 Shi, Y., Yamaguchi, Y.: A high-resolution and multi-year emissions inventory for  
769 biomass burning in Southeast Asia during 2001-2010. *Atmospheric Environment*,  
770 98, 8-16, <http://dx.doi.org/10.1016/j.atmosenv.2014.08.050>, 2014.

771 Singh H.B., Hara D.O., Herlth D., Sachse W., Blake D.R., Bradshaw J.D., Kanakidou  
772 M., Crutzen P. J., Acetone in the atmosphere: Distribution, sources, and sink., *J.*  
773 *Geophys. Res.*, 99,1805-1819, 1994.

774 Stein, A. F., R. R. Draxler, G. D. Rolph, B. J. B. Stunder, M. D. Cohen, and F.  
775 Ngan. : NOAA’s HYSPLIT Atmospheric Transport and Dispersion Modeling  
776 System, *Bulletin of the American Meteorological Society* 96, 12 (2015): 2059-  
777 2077, <https://doi.org/10.1175/BAMS-D-14-00110.1>, 2021.

778 Stockwell, W. R., Middleton, P., Chang, J. S., and Tang, X.: The second generation  
779 regional acid deposition model chemical mechanism for regional air quality  
780 modeling, *J. Geophys. Res.*, 95, 16343–16367, 1990.

781 Stockwell, W. R., Kirchner F., Kuhn M.: A new mechanism for regional atmospheric

782 chemistry modeling, *J. Geophys. Res.*, 102, 25847–25879, 1997.

783 Talbot, R., Dibb, J., Scheuer E., Seid G., Russo R., Sandholm S., Tan D., Singh H.,  
784 Blake D., Blake N., Atlas E., Sachse G., Jordan C., Avery M., 2003: Reactive  
785 nitrogen in Asian continental outflow over the western Pacific: Results from the  
786 NASA Transport and Chemical Evolution over the Pacific (TRACE-P) airborne  
787 mission. *J. Geophys. Res.*, 108 (D20), doi:10.1029/2002JD003110, 2003.

788 Tang, Y., Carmichael, G. R., Woo, Jung-Hun, Thongboonchoo N., Kurata, G., Uno, I.,  
789 Streets D. G., et al.: Influences of biomass burning during the Transport and  
790 Chemical Evolution Over the Pacific (TRACE-P) experiment identified by the  
791 regional chemical transport model, *J. Geophys. Res.*, 108(D21), 8824, 2003.

792 Wiedinmyer, C., Akagi, S. K., Yokelson, R. J., Emmons, L. K., Al-Saadi, J.A., Orlando,  
793 J. J., and Soja, A. J.: The Fire INventory from NCAR (FINN): a high resolution  
794 global model to estimate the emissions from open burning, *Geosci. Model Dev.*, 4,  
795 625-641, doi:10.5194/gmd-4-625-2011, 2011.

796 Xu, R., Tie, X., Li, G., Zhao, S., Cao, J., Feng T., Long X., Effect of biomass burning  
797 on black carbon (BC) in South Asia and Tibetan Plateau: The analysis of WRF-Chem  
798 modeling. *Science of the Total Environment* › 645,901-912., 2018.

799 Yadav, I. C., Devi, N. L., Li, J., Syed, J. H., Zhang, G., Watanabe, H.: Biomass burning  
800 in Indo-China peninsula and its impacts on regional air quality and global climate  
801 change-a review. *Environmental Pollution*, 227, 414-427, 2017.

802 Zhao, C., Liu, X., Leung, L. R. and Hagos, S.: Radiative impact of mineral dust on  
803 monsoon precipitation variability over West Africa. *Atmos. Chem. Phys.*, 11, 1879-  
804 1893, 2011.

805  
806  
807  
808  
809  
810  
811  
812  
813  
814  
815  
816  
817  
818  
819

820 Table 1: WRF-Chem model configuration and physics and chemistry options in this  
 821 study. (RRTMG=Rapid Radiative Transfer Model for General Circulation Models;  
 822 FINN=Fire Inventory from National Center for Atmospheric Research)  
 823

Resolution	10km
Microphysics	Lin
Cumulus parameterization	Grell 3D ensemble scheme
Planetary Boundary Layer	Mellor-Yamada-Janjic TKE scheme
Longwave radiation	RRTMG
Shortwave radiation	RRTMG
Fire emissions	FINN V1.5
Anthropogenic emissions	MICS-Asia III(2010) + Taiwan Emission Data System ver 9.0 (2013)
Biogenic emissions	MEGAN V2.04
Chemistry option	RACM Chemistry with MADE/VBS aerosols using KPP library along with the volatility basis set (VBS) used for Secondary Organic Aerosols
Photolysis option	Madronich
wet scavenging	On , (Neu and Prather, 2012)
Cloud chemistry	On,
feedback from the aerosols to the radiation schemes	On
the time interval for calling the biomass-burning plume rise subroutine	180 min
feedback from the parameterized convection to the atmospheric radiation and the photolysis schemes	On
Subgrid-scale wet scavenging	on
Subgrid aqueous chemistry	on

824  
 825  
 826  
 827  
 828  
 829  
 830  
 831  
 832

833 Table 2 Observed and simulated mean values for bias (BIAS), root mean square error  
 834 (RMSE), and correlation coefficients (R) for EMerGe HALO flights on 17 and 19  
 835 March 2018. KET\*: the observed Acetone is applied to compare with simulated ketones  
 836 (KET).

	OBS_ave	SIM_ave	BIAS	RMSE	R
THETA(K)	304.8	304.2	-0.6	1.1	0.99
WS(m/s)	9.1	8.5	-0.6	2.0	0.94
RH(%)	63.6	62.9	-0.6	10.7	0.92
OA( $\mu\text{g}/\text{m}^3$ )	1.2	1.4	0.3	1.1	0.61
BC( $\mu\text{g}/\text{m}^3$ )	0.4	0.5	0.1	0.4	0.74
SO <sub>4</sub> <sup>2-</sup> ( $\mu\text{g}/\text{m}^3$ )	1.1	2.5	1.4	2.3	0.42
NO <sub>3</sub> <sup>-</sup> ( $\mu\text{g}/\text{m}^3$ )	0.2	0.6	0.5	2.1	0.31
NH <sub>4</sub> <sup>+</sup> ( $\mu\text{g}/\text{m}^3$ )	0.4	0.7	0.3	1.2	0.49
CO(ppb)	170.8	191.8	20.9	72.8	0.45
SO <sub>2</sub> (ppb)	0.2	0.7	0.4	1.2	0.55
O <sub>3</sub> (ppb)	59.7	63.2	3.5	14.4	0.43
NO <sub>x</sub> (ppb)	0.2	0.2	0.0	0.2	0.72
NO <sub>y</sub> (ppb)	1.2	2.6	1.3	2.3	0.03
KET* (ppb)	1.4	1.6	0.1	0.9	0.59
TOL(ppb)	0.1	0.1	0.0	0.1	0.75
XYL(ppb)	0.1	0.0	0.0	0.1	0.40
HCHO(ppb)	0.1	0.7	0.5	0.7	0.51
HONO(ppb)	10.5	1.0	-9.4	15.3	0.56

837

838 Table 3 Observed and simulated mean values at an elevation between 2 km and 4 km  
 839 for bias (BIAS), root mean square error (RMSE), and correlation coefficients (R) during  
 840 EMeRGe HALO flights on 17 and 19 March 2018. KET\*: the observed Acetone is  
 841 applied to compare with simulated ketones (KET).

	OBS_ave	SIM_ave	BIAS	RMSE	R
THETA(K)	307.5	306.7	-0.7	0.9	0.98
WS(m/s)	8.2	7.9	-0.3	1.7	0.93
RH(%)	55.8	56.0	0.2	7.6	0.96
OA( $\mu\text{g}/\text{m}^3$ )	1.3	1.6	0.3	0.7	0.85
BC( $\mu\text{g}/\text{m}^3$ )	0.4	0.7	0.2	0.5	0.79
SO <sub>4</sub> <sup>2-</sup> ( $\mu\text{g}/\text{m}^3$ )	0.8	2.5	1.7	2.1	0.20
NO <sub>3</sub> <sup>-</sup> ( $\mu\text{g}/\text{m}^3$ )	0.1	0.0	-0.1	0.3	0.13
NH <sub>4</sub> <sup>+</sup> ( $\mu\text{g}/\text{m}^3$ )	0.4	0.4	0.0	0.2	0.52
CO(ppb)	164.4	228.7	64.2	85.4	0.58
SO <sub>2</sub> (ppb)	0.0	0.7	0.6	0.9	0.07
O <sub>3</sub> (ppb)	60.1	72.6	12.5	15.0	0.55
NO <sub>x</sub> (ppb)	0.1	0.2	0.0	0.1	0.53
NO <sub>y</sub> (ppb)	1.0	3.6	2.6	3.0	0.51
KET*(ppb)	1.5	2.0	0.5	1.0	0.70
TOL(ppb)	0.1	0.0	0.0	0.1	0.16
XYL(ppb)	0.0	0.0	0.0	0.0	-0.17
HCHO(ppb)	0.1	0.7	0.6	0.7	0.25
HONO(ppt)	6.0	0.6	-5.4	7.2	0.23

842  
 843  
 844  
 845  
 846  
 847  
 848  
 849  
 850  
 851  
 852  
 853  
 854  
 855  
 856  
 857  
 858  
 859  
 860



861

862 Table 4: Simulated biomass burning contribution (with and without BB emission in  
863 Indochina) in percentage (%) on 17 and 19 March, 2018 for different regions: SCA,  
864 TWA, ECSA as shown in Figure 1a

865

Average	SCA		TWA		ECSA	
	< 1KM	2-4KM	< 1KM	2-4KM	< 1KM	2-4KM
NO <sub>y</sub>	13.6	72.2	39.7	83.3	14.8	69.9
NO <sub>x</sub>	-1.3	58.1	2.9	71.1	1.4	51.0
PM <sub>2.5</sub>	7.5	46.0	15.1	55.6	7.6	34.4
OA	5.3	41.4	7.5	48.1	4.4	28.5
BC	8.0	79.5	16.4	81.4	6.8	47.9
OH	14.7	43.8	24.1	67.4	9.2	48.3
O <sub>3</sub>	18.8	34.2	23.2	39.2	9.2	31.3
CO	9.8	31.7	21.9	38.4	11.1	32.2
KET	6.2	17.8	9.5	27.5	7.2	24.7
HCHO	-4.2	9.8	-4.8	20.6	-4.7	10.4
HO <sub>2</sub>	8.8	2.6	15.2	35.8	6.3	23.2
J(O <sup>1</sup> D)	-1.5	-0.8	-1.1	0.5	-1.5	-1.0

866

867

868

869

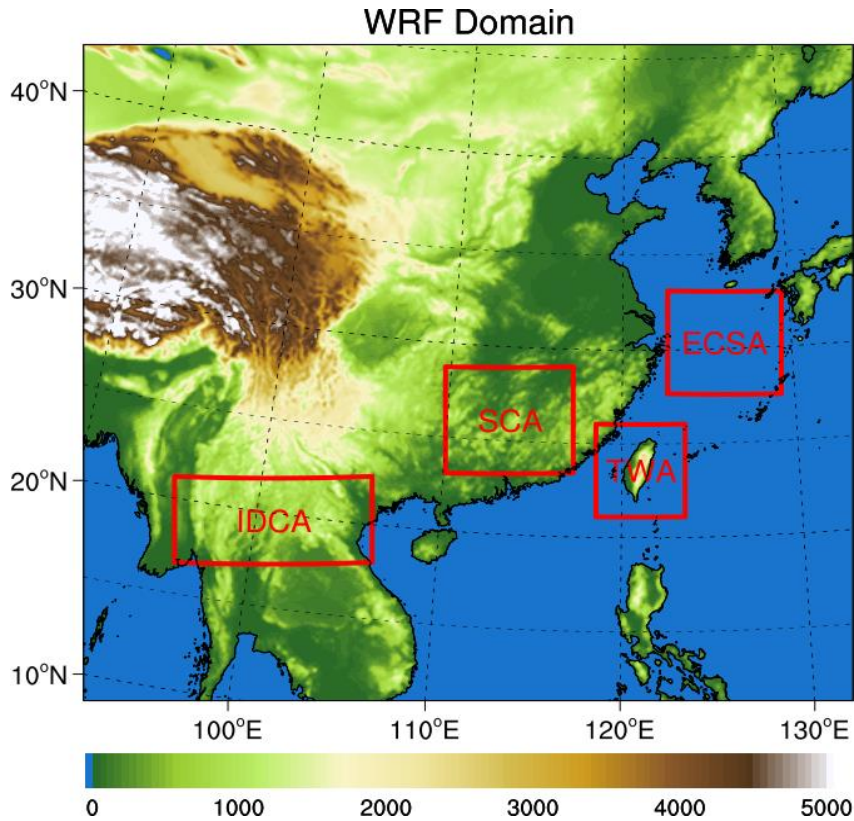
870

871

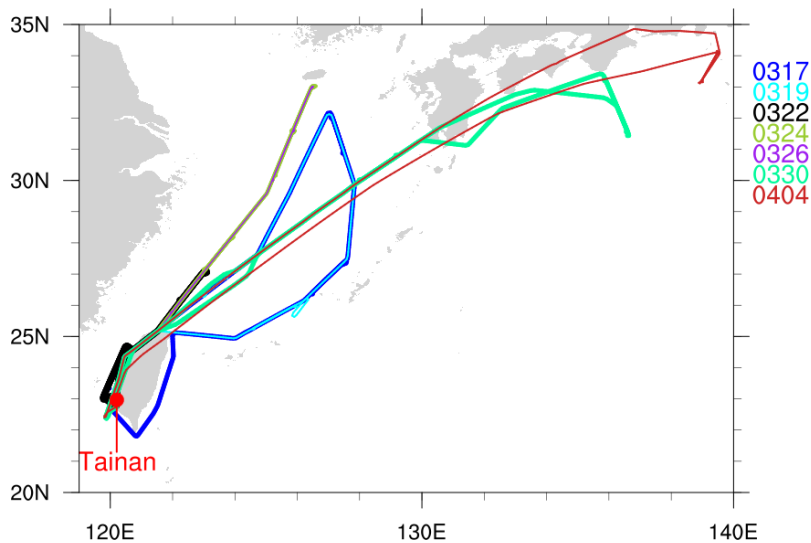
872

873

874 (a)



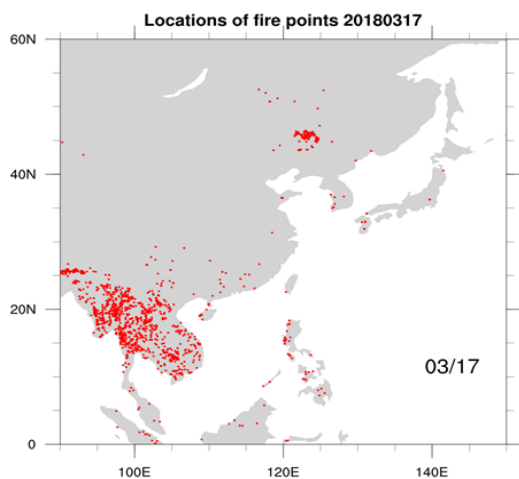
892 (b)



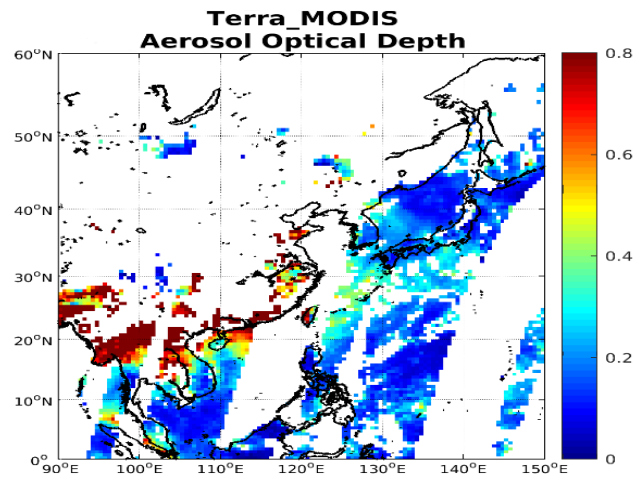
904 Figure 1 (a) Configuration of Weather Research and Forecasting model domain,  
905 topography, and location of proposed study areas in East Asia, namely IDCA (Indochina  
906 area), SCA (southern China area), TWA (Taiwan area) and ECSA (East China Sea area,  
907 respectively. (b) The HALO flights on 17, 19, 22, 24, 26, 30 March, and 04 April  
908 during EMERGe Asia campaign. Different colors indicated different flights over East  
909 Asia. Maps and plots were produced using NCAR Command Language (NCL) version  
910 6.6.2.

911

912 (a)

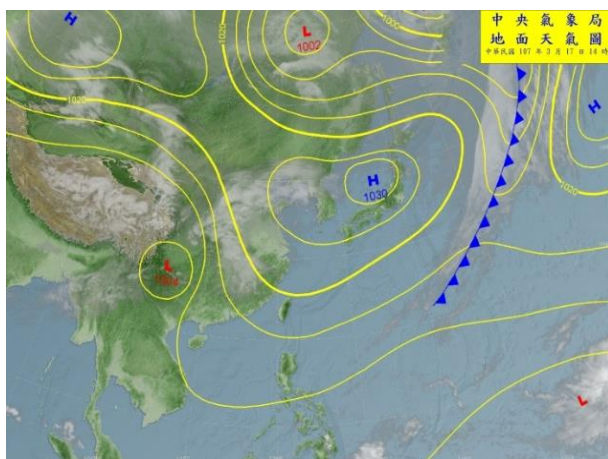


(b)

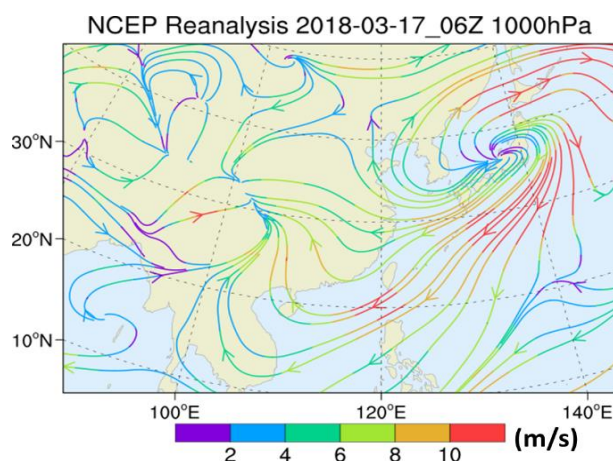


913

914 (c)



(d)

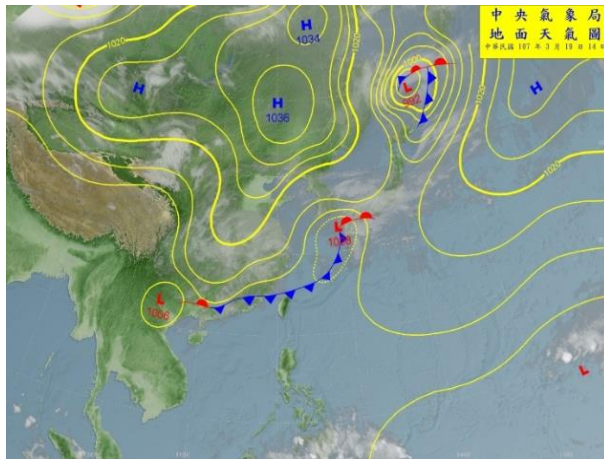


915

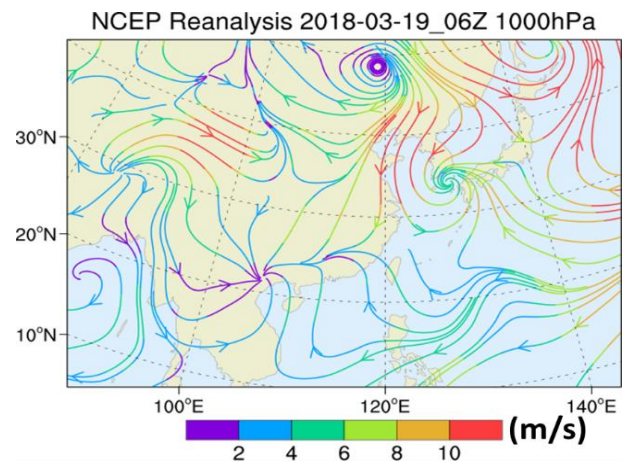
916 Fig.2 (a) MODIS fire hot spots on 17 March 2018 (source: [https://modis-](https://modis-fire.umd.edu/guides.html)  
 917 [fire.umd.edu/guides.html](https://modis-fire.umd.edu/guides.html)) and (b) Composited Aerosol Optical Depth (AOD) from  
 918 MODIS onboard NASA Terra satellite. The Collection 6.1 AOD is downloaded from  
 919 NASA Earth Data website (<https://www.earthdata.nasa.gov/learn/find-data>), and  
 920 composited for 0110, 0115, 0120, 0125, 0130, 0250, 0255, 0300, 0305, 0310, 0430,  
 921 0435, 0440, 0445, 0610, 0615, 0620, 0745 and 0750UTC data granules on 17 March  
 922 2018. (c) weather Chart at 06:00 UTC on 17 March 2018 (d) 1000 hPa streamlines at  
 923 06:00 UTC, 17 March 2018 (e) and (f) same as (c) and (d) but on 19 March 2018 ;(g)  
 924 700 hPa streamlines at 06:00 UTC, on 17 March 2018 (h) 700 hPa geopotential height  
 925 at 06:00 UTC, on 17 March 2018; (i) and (j) same as (g) and (h) but on 19 March  
 926 2018.

927 Near-surface weather charts and satellite images were provided by Central Weather  
 928 Bureau (CWB) Taiwan. The near-surface and 700 hPa streamlines and geopotential  
 929 height were deduced from NCEP Reanalysis data. Maps and plots were produced using  
 930 NCAR Command Language (NCL) version 6.6.2.

931 (e)



(f)

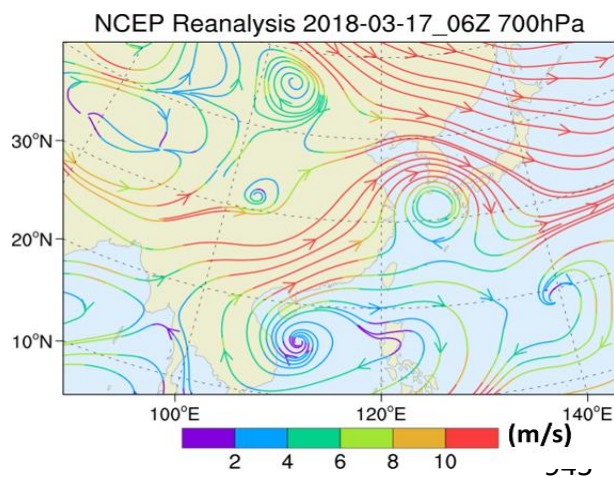


932

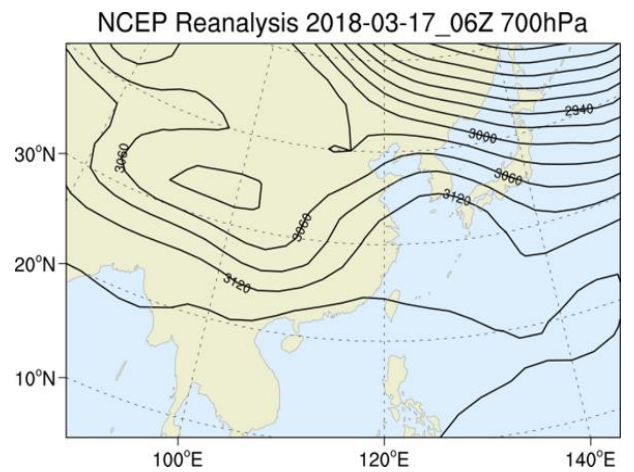
933

934 (g)

935



(h)



946

947

948

949 Figure 2 e-h continued

950

951

952

953

954

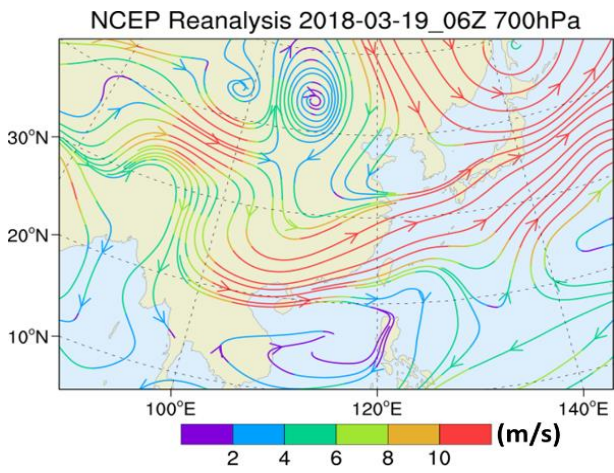
955

956

957

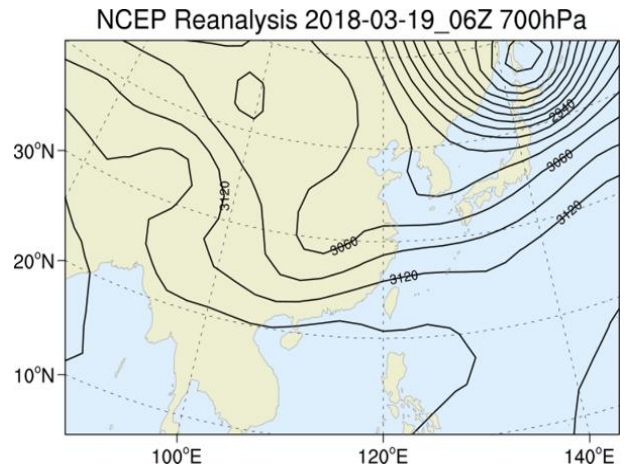
958

959 (i)  
960  
961



962

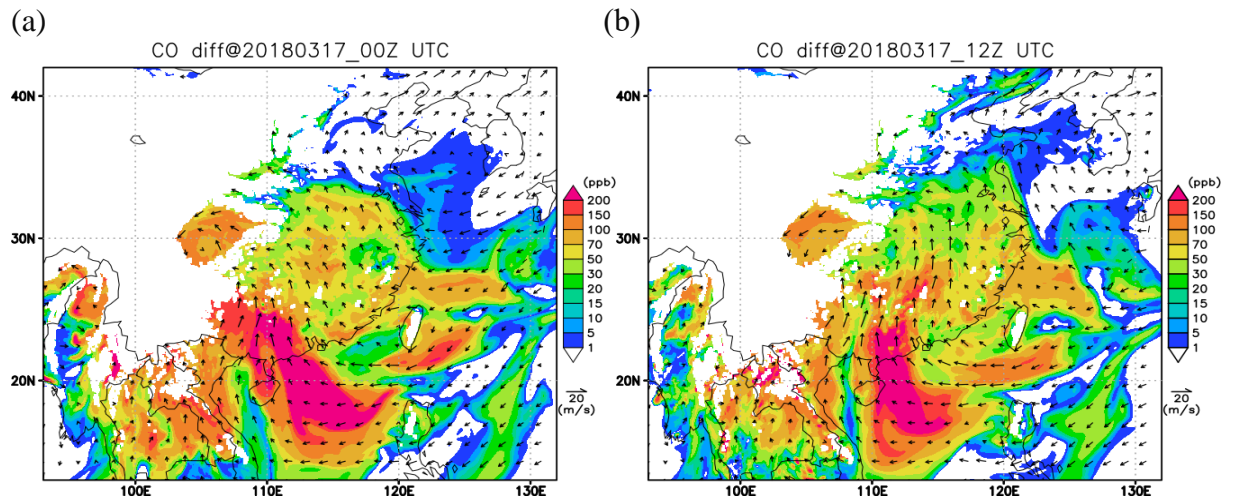
(j)



963  
964  
965  
966  
967  
968  
969  
970  
971  
972  
973  
974  
975  
976  
977  
978  
979  
980  
981  
982  
983  
984  
985  
986  
987

Fig. 2 i-j continued

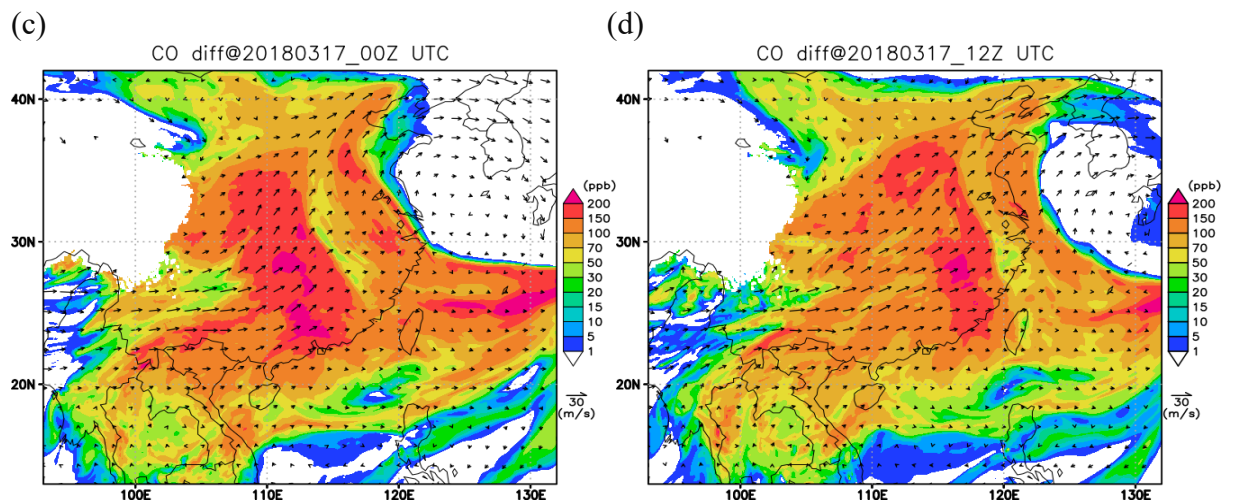
988



989

990

991



992

993

994

995 Fig 3 a-d : Simulated wind field ( $\text{m s}^{-1}$ ) distribution and concentration (unit: ppb)

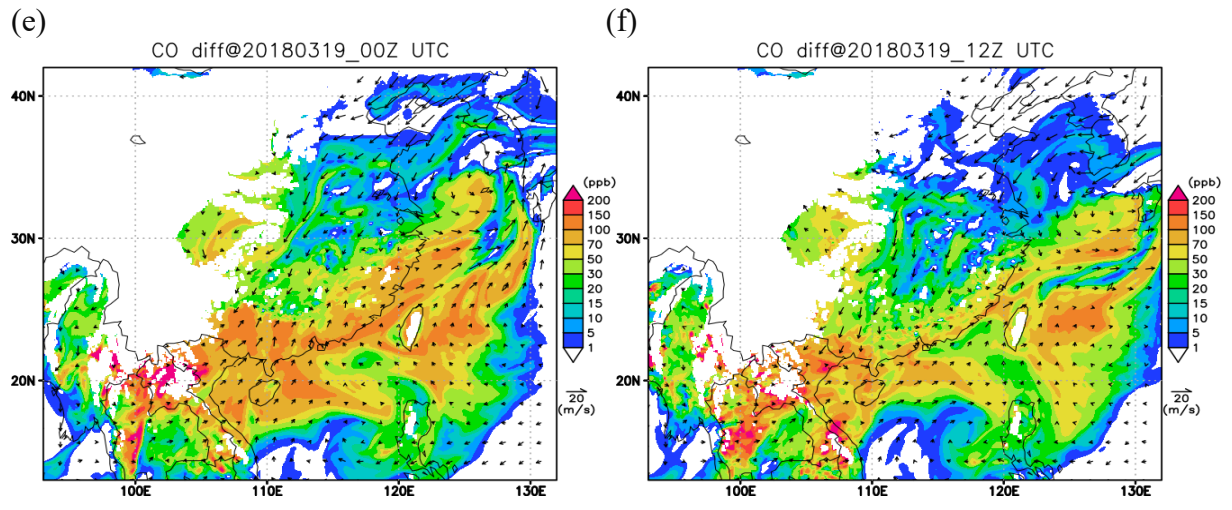
996 difference with and without BB emission for CO on 17 March, 2018 at 00:00 UTC (a,

997 c) and 12:00 UTC (b, d) for 1km altitude (a, b) and 3km altitude (c, d). (unit:ppb)

998

999

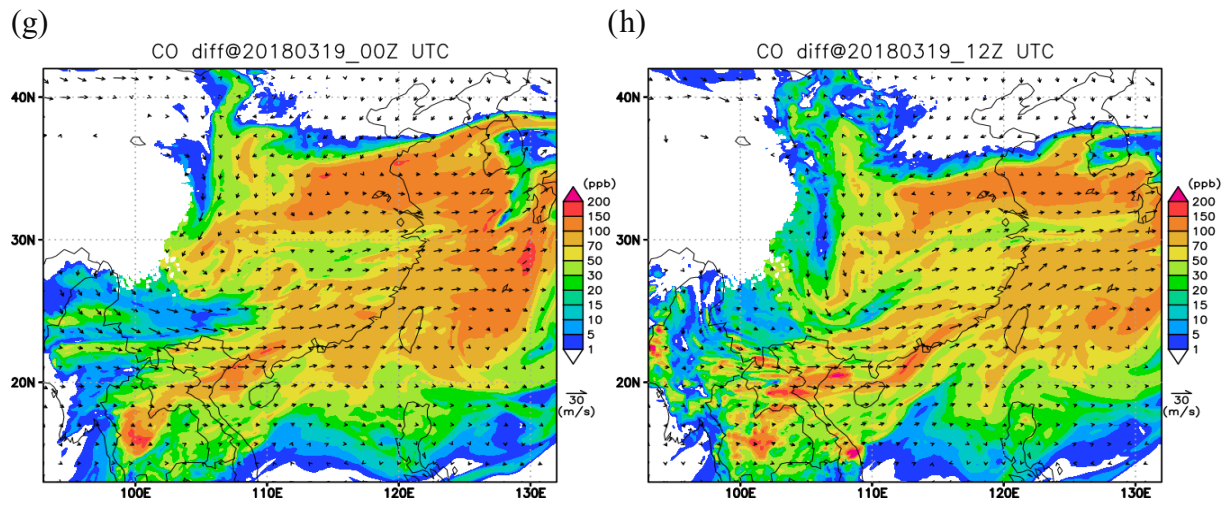
1000



1001

1002

1003



1004

1005 Fig 3 e-h: Simulated wind field ( $\text{m s}^{-1}$ ) and concentration (unit: ppb) difference with

1006 and without BB emission for CO on 19 March, 2018 at 00:00 UTC (e, g) and 12:00

1007 UTC (f, h) for 1km altitude (e, f) and 3km altitude (g, h).

1008

1009

1010

1011

1012

1013

1014

1015

1016

1017

1018

1019 (a)

1020

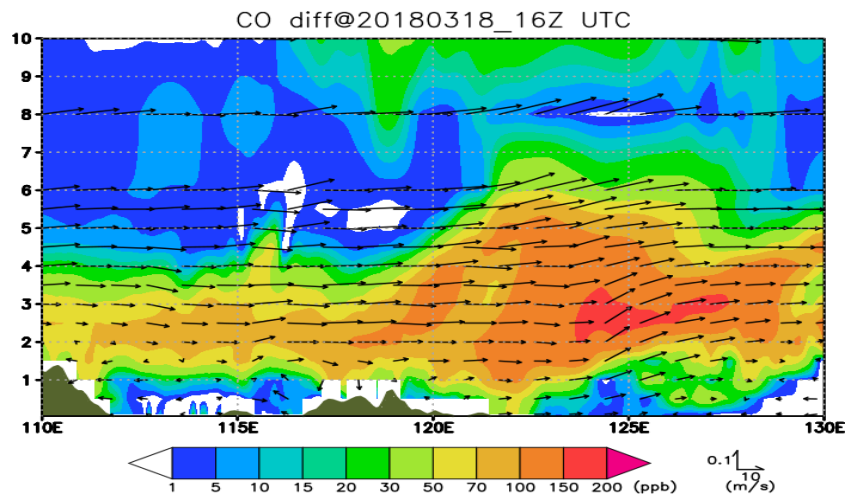
1021

1022

1023

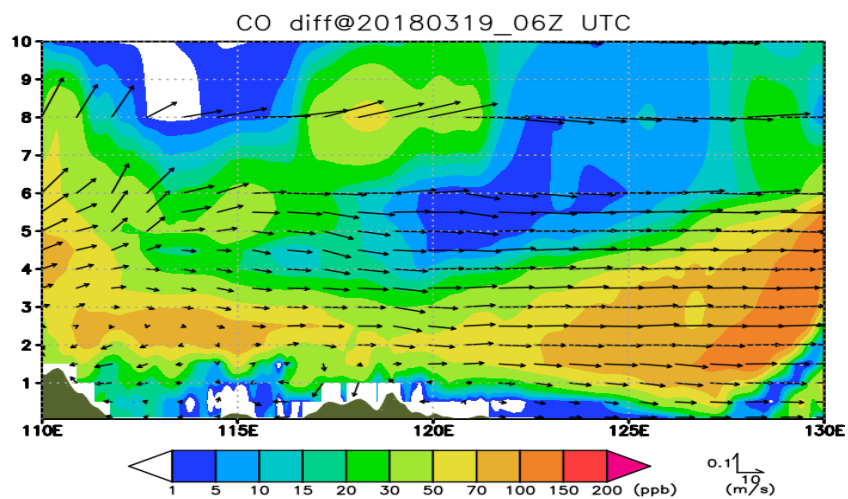
1024

1025



1026

1027 (b)



1028

1029

1030

1031

1032 Fig. 4 Simulated wind field ( $\text{m s}^{-1}$ ) distribution and the concentration (ppb) difference

1033 between with and without BB emission for CO at cross-section  $30^\circ\text{N}$  (a) 16:00 UTC

1034 18 March 2018 (b) 06:00 UTC, 19 March 2018. Wind vectors represent along section

1035 winds, with scales shown at the down-right corner of plot (unit:  $\text{m s}^{-1}$ )

1036

1037

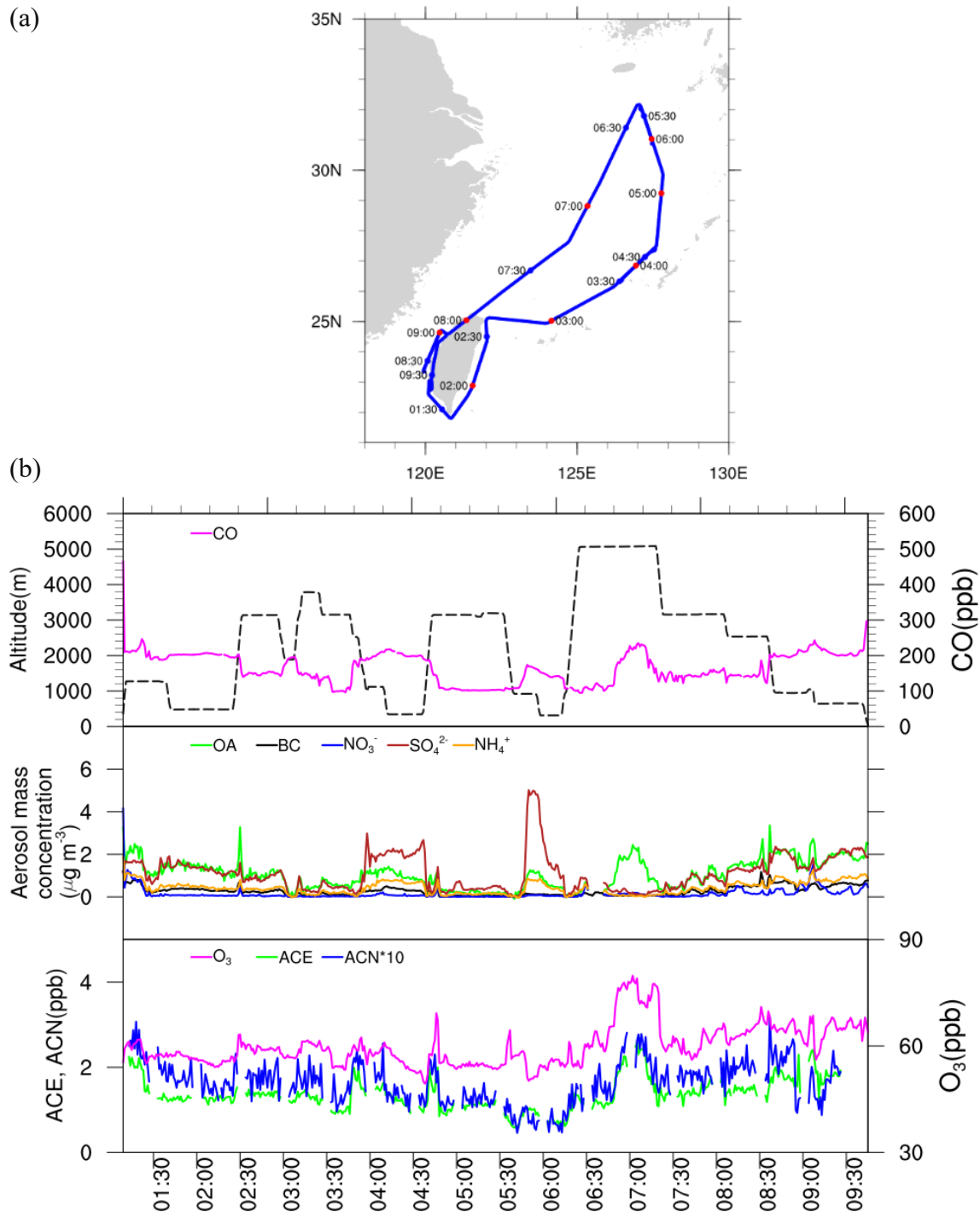
1038

1039

1040



1041 (a)  
 1042  
 1043  
 1044  
 1045  
 1046  
 1047  
 1048  
 1049  
 1050  
 1051  
 1052 (b)



1053  
 1054  
 1055  
 1056  
 1057  
 1058  
 1059  
 1060  
 1061

Fig. 5 (a) The HALO flight and detailed locations on 17 March 2018. (b) Flight altitude and 1-min mean of observed concentrations for CO (upper), Organic aerosol (OA), BC aerosol (BC),  $\text{SO}_4^{2-}$ ,  $\text{NO}_3^-$ ,  $\text{NH}_4^+$  (middle),  $\text{O}_3$ , acetone (ACE) and acetonitrile (ACN) (bottom) on 17 March. (c) The observed  $\text{SO}_4^{2-}$  mass concentration by HALO along with height-latitude variations on 17 March 2018 (d) The observed OA mass concentration by HALO along with height-latitude variations on 17 March 2018 (e) Result of the HYSPLIT model backward trajectory analysis started at the location of the HALO flight path at 02:00, 04:00, 06:00, 09:00 UTC on 17 March 2018.

1062 (c)

1063

1064

1065

1066

1067

1068

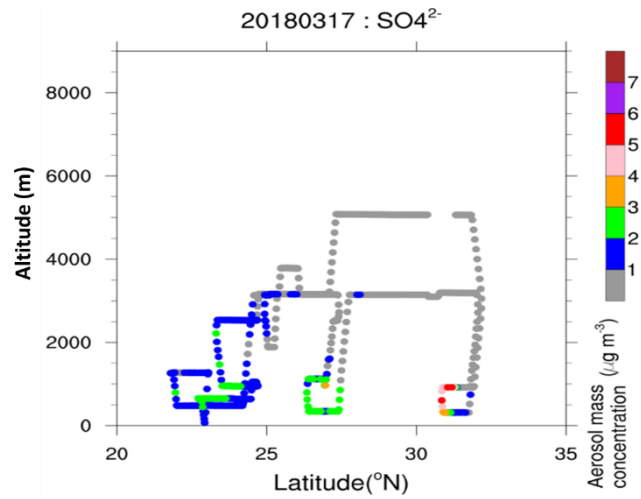
1069

1070

1071

1072

1073



1074 (d)

1075

1076

1077

1078

1079

1080

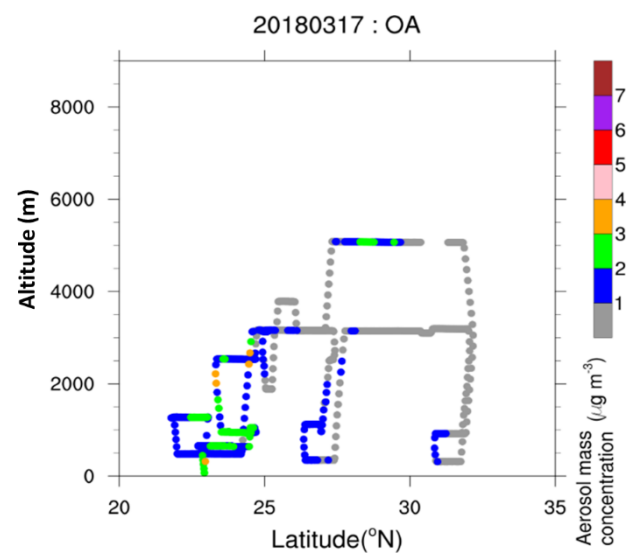
1081

1082

1083

1084

1085



1086 (e)

1087

1088

1089

1090

1091

1092

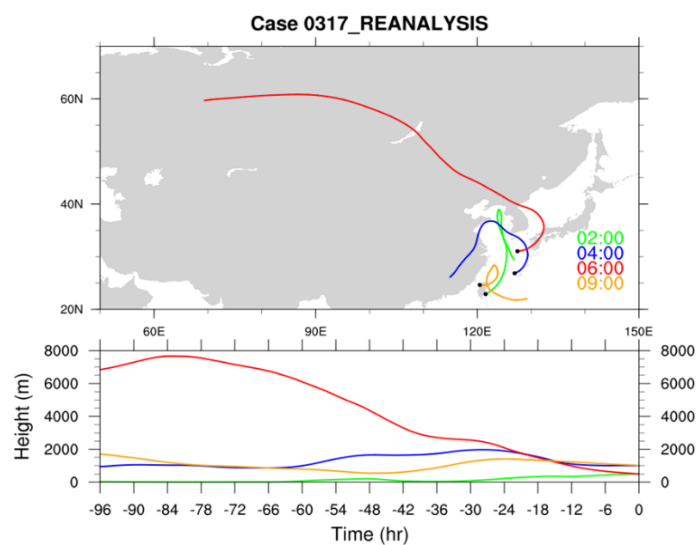
1093

1094

1095

1096

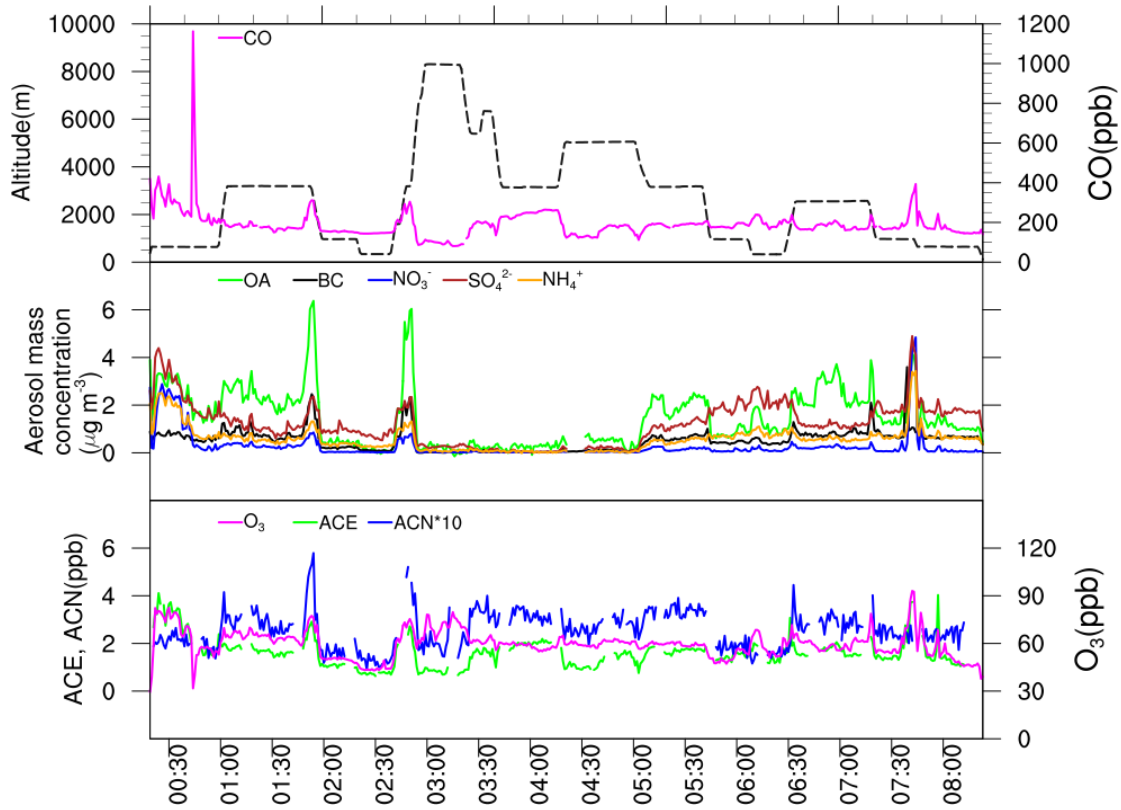
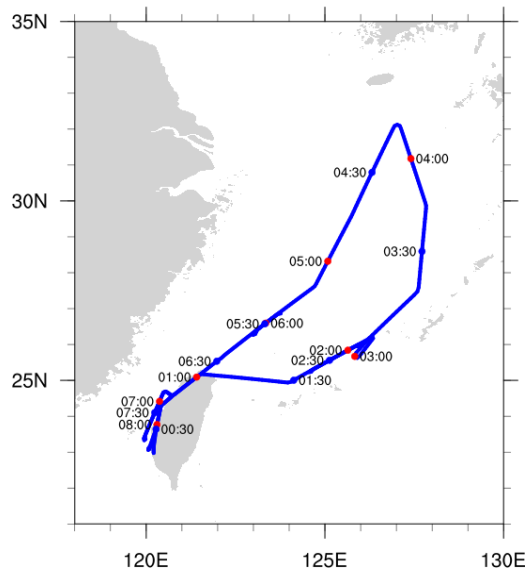
1097



1098 Figure 5 c-e

1099

11100 (a)  
 11101  
 11102  
 11103  
 11104  
 11105  
 11106  
 11107  
 11108  
 11109  
 11110  
 11111  
 11112 (b)



11113  
 11114  
 11115  
 11116  
 11117  
 11118  
 11119  
 11120  
 11121

Figure 6 (a) The HALO flight and detailed locations on 19 March. (b) Flight altitude and 1-min mean of observed concentrations for CO (upper), Organic aerosol (OA), BC aerosol (BC),  $\text{SO}_4^{2-}$ ,  $\text{NO}_3^-$ ,  $\text{NH}_4^+$  (middle),  $\text{O}_3$ , acetone (ACE) and Acetonitrile (ACN) (bottom) on 19 March 2018. (c) The observed  $\text{SO}_4^{2-}$  mass concentration by HALO along with height-latitude variations on 19 March 2018 (d) The observed OA mass concentration by HALO along with height-latitude variations on 19 March 2018 (e) Result of the HYSPLIT model backward trajectory analysis started at the location of the HALO flight path at 02:00, 04:00, 05:00, 07:00 UTC on 19 March 2018.

1122 (c)

1123

1124

1125

1126

1127

1128

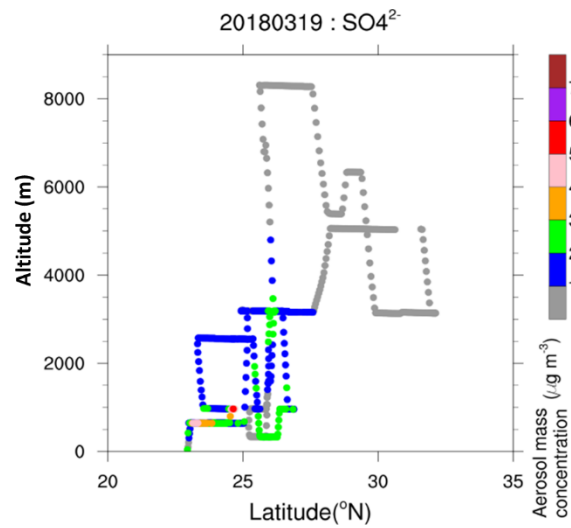
1129

1130

1131

1132

1133



1134 (d)

1135

1136

1137

1138

1139

1140

1141

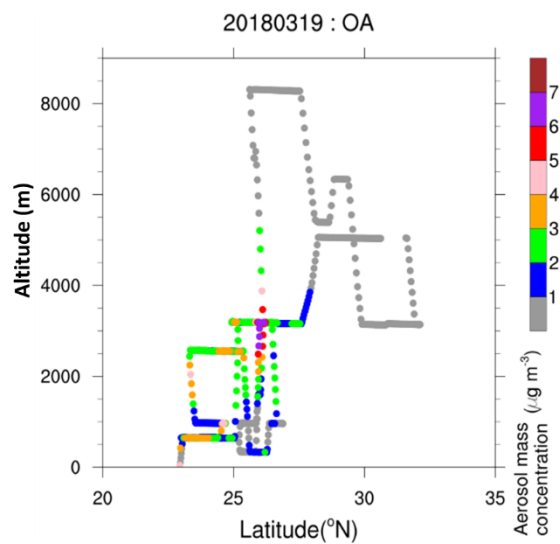
1142

1143

1144

1145

1146



1147 (e)

1148

1149

1150

1151

1152

1153

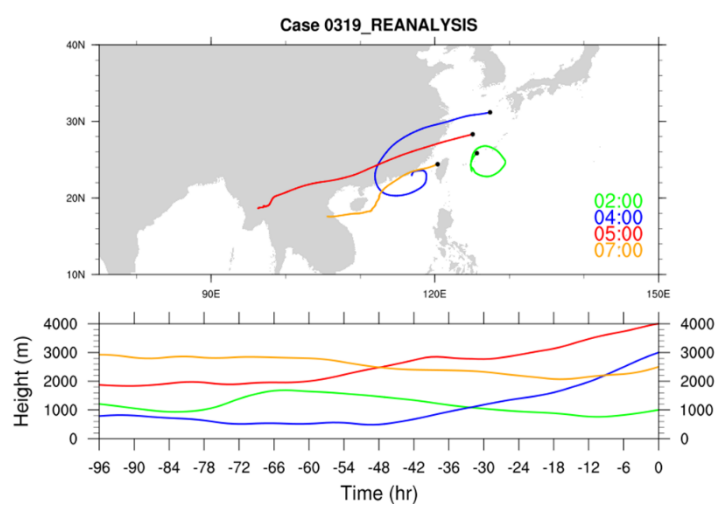
1154

1155

1156

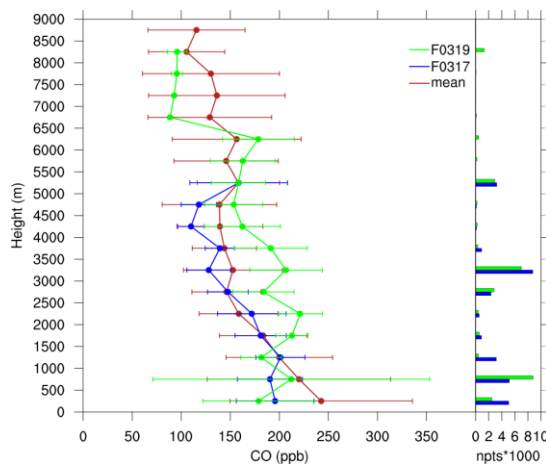
1157

1158

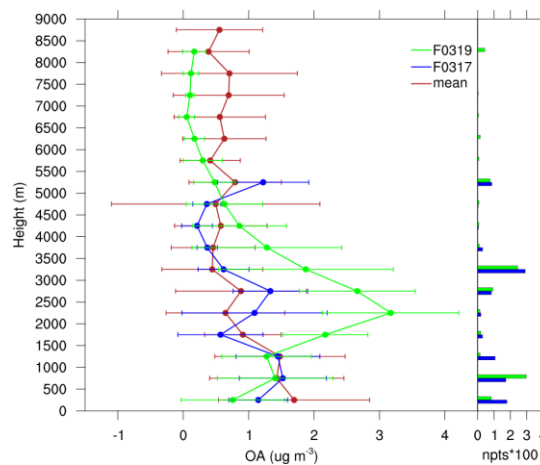


1159 Figure 6 c-e

1160 (a)  
1161

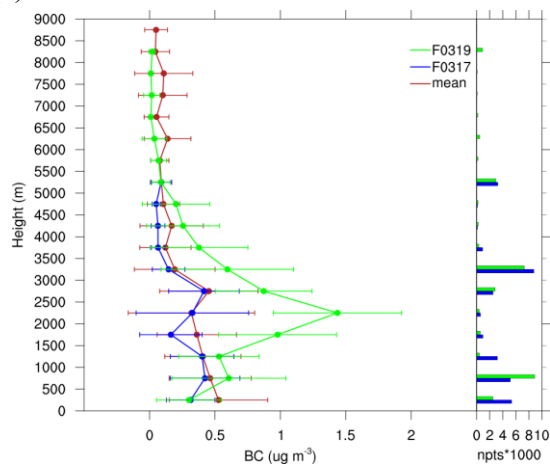


(b)

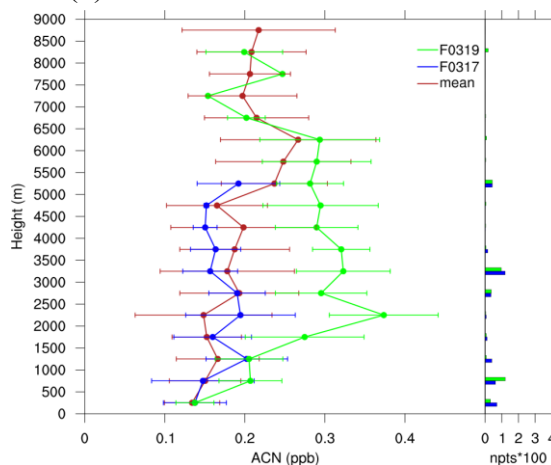


1162

1163 (c)



(d)



1164

1165

1166

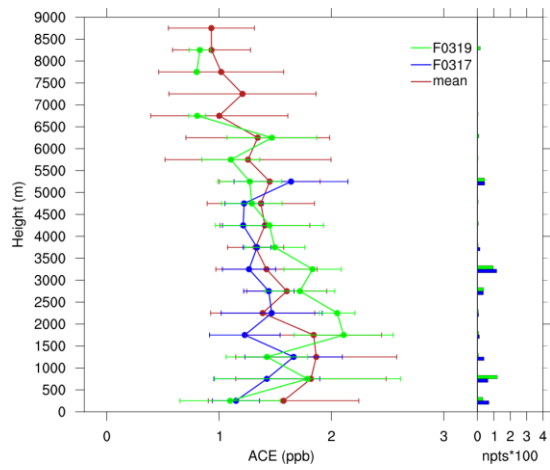
1167

1168 Fig.7 Observed vertical distribution calculated as 1-min mean and 500 m interval with  
1169 one standard deviation of the concentrations for the mean profiles (red) (including 17,  
1170 19, 22, 24, 26, 30 March, and 04 April 2018) and flights on 17 (blue) and 19 (green)  
1171 March 2018. (a) CO (b) OA (c) BC (d) Acetonitrile (ACN) (e) Acetone (ACE) (f) O<sub>3</sub>  
1172 (g) J (O<sup>1</sup>D) (h) NO<sub>y</sub>. The number of data points is shown in the right panel.

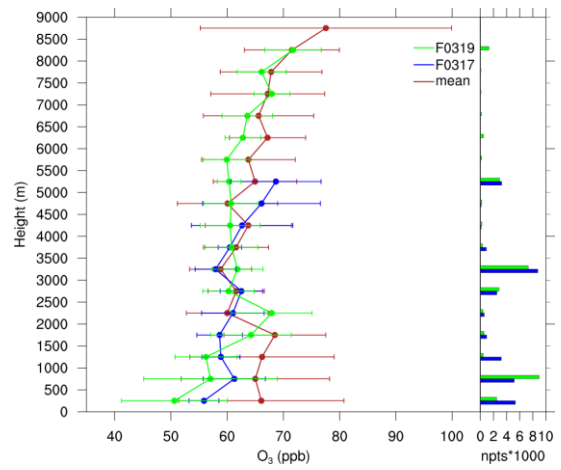
1173

1174

1175 (e)

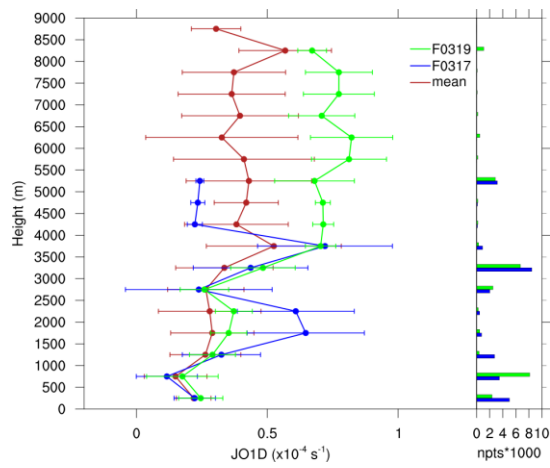


(f)

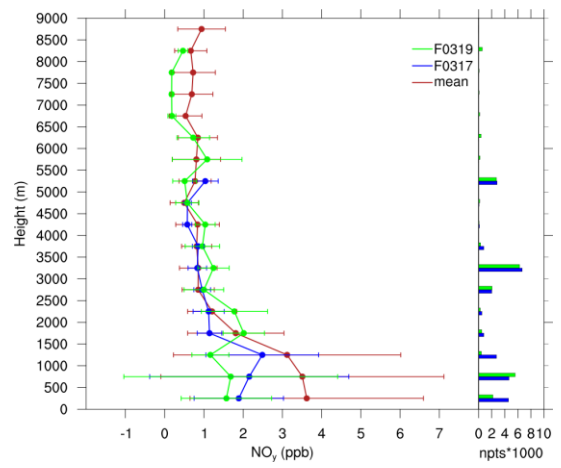


1176

1177 (g)



(h)



1178

1179

1180

1181

1182

1183

1184 Figure 7 continued

1185

1186

1187

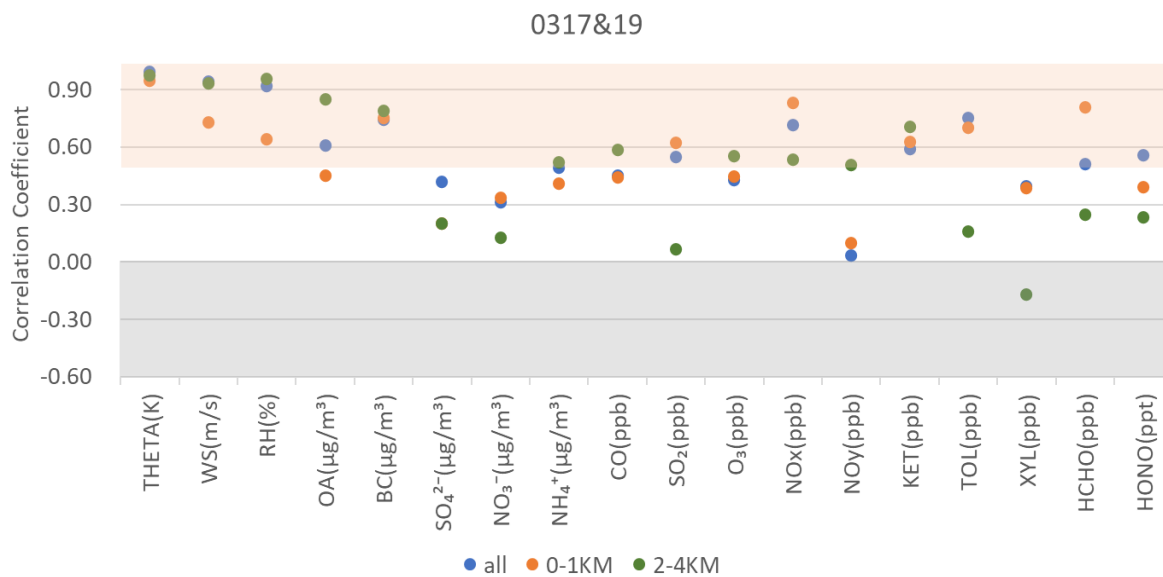
1188

1189

1190

1191

1192



1193

1194

1195

1196 Fig. 8 Correlation Coefficient (R) between observation and simulation along with the  
1197 HALO flights at the elevations 0-1 km, 2-4 km, and the whole track (all) on 17 and 19  
1198 March 2018.

1199

1200

1201

1202

1203

1204

1205

1206

1207

1208

1209

1210

1211

1212

1213

1214

1215

1216

1217

1218 (a)

1219

1220

1221

1222

1223

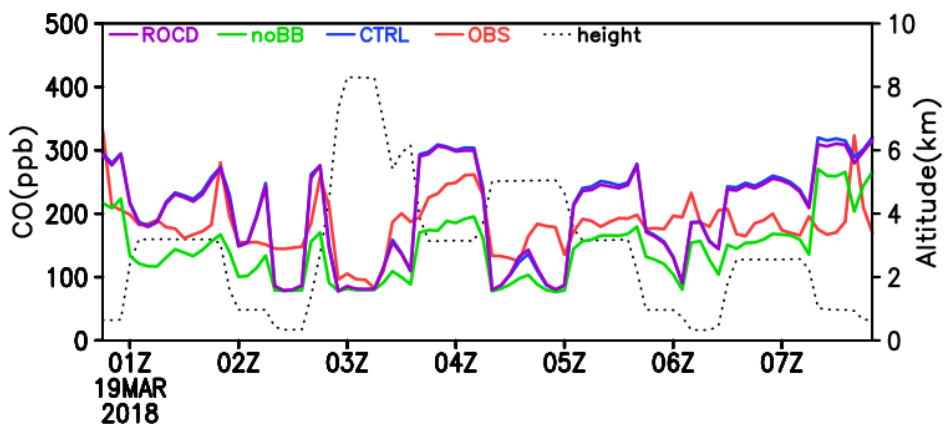
1224

1225

1226

1227

1228



1229 (b)

1230

1231

1232

1233

1234

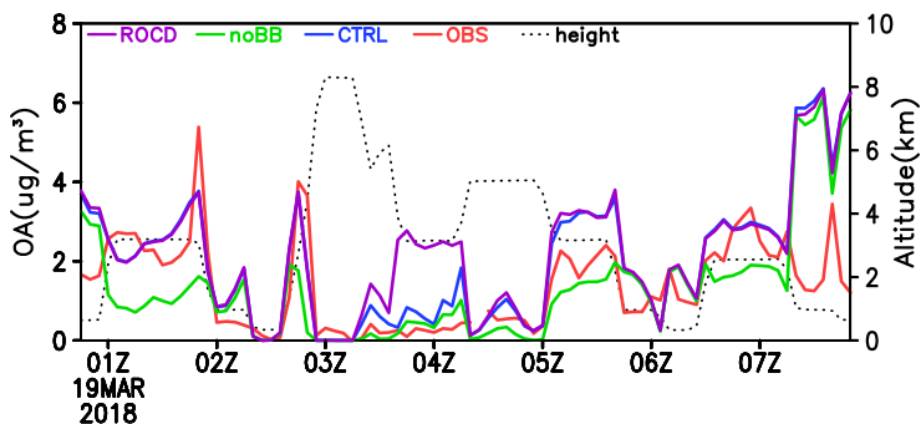
1235

1236

1237

1238

1239



1240 (c)

1241

1242

1243

1244

1245

1246

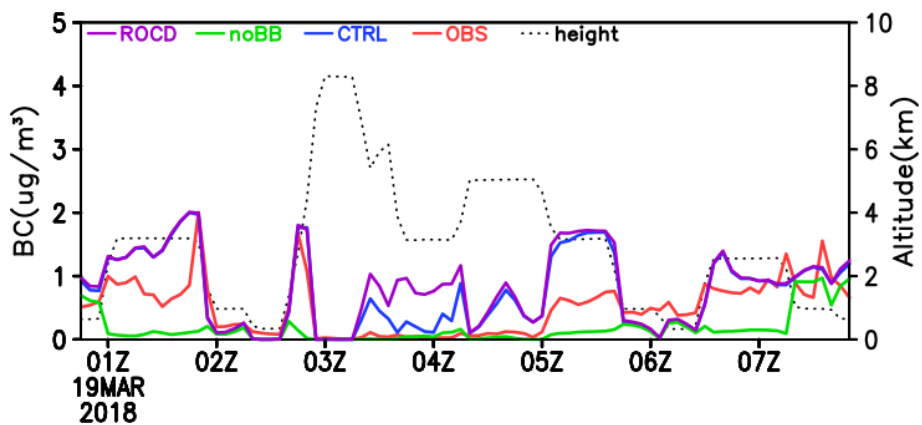
1247

1248

1249

1250

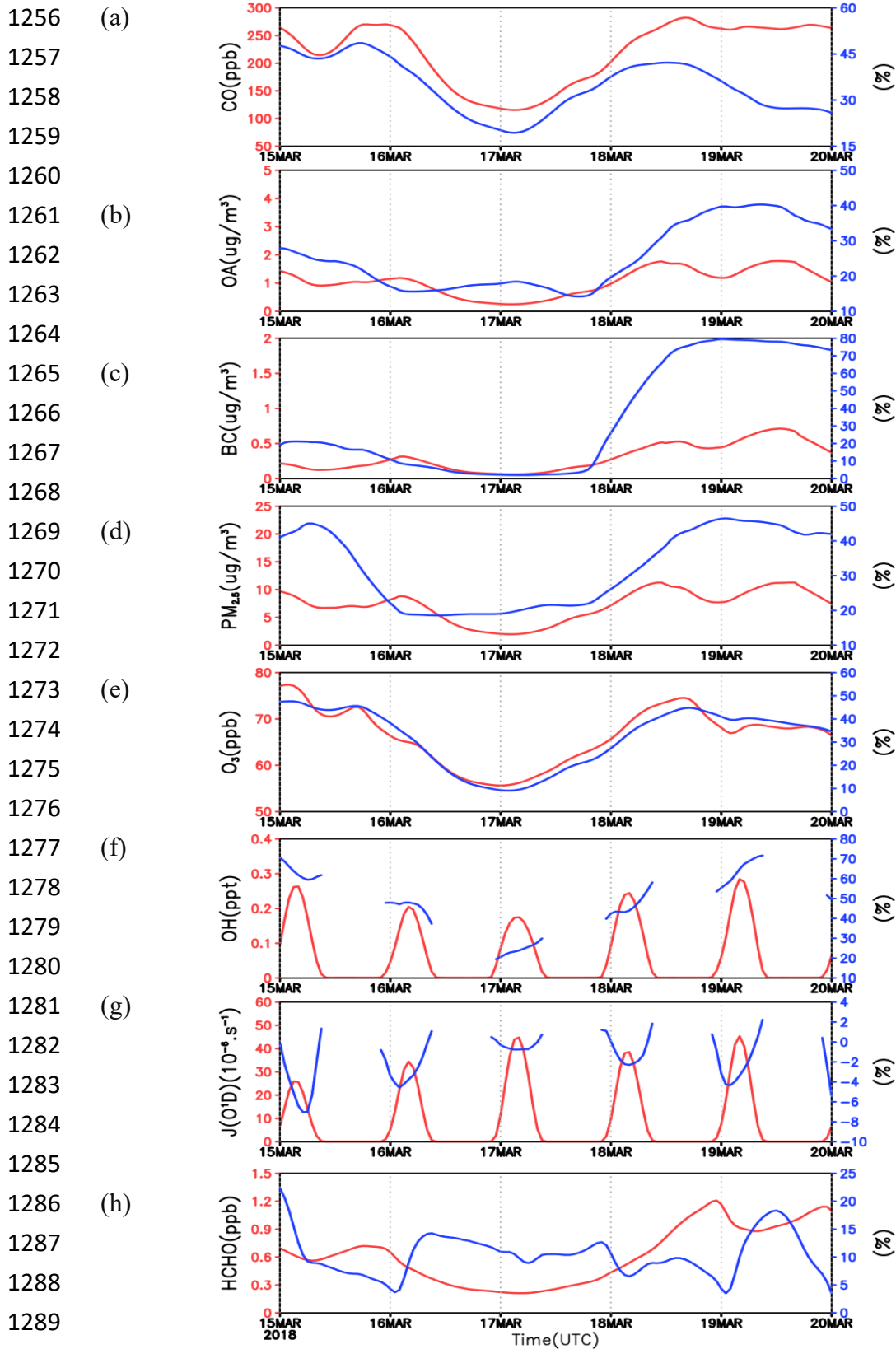
1251



1252 Fig.9 Observed (OBS, red) and simulated concentration (CTRL, blue), and the simulation  
1253 without indirect effect (ROCD, purple), without BB emission (noBB, green) along with the  
1254 flight altitude for (a) CO (ppb) (b) OA ( $\mu\text{g m}^{-3}$ ) (c) BC ( $\mu\text{g m}^{-3}$ ) on 19 March 2018.

1255





1291 Figure 10 Hourly variation of simulated mean concentration (red) and contributed by  
 1292 BB (%) (blue) between 2 km and 4 km over the region ECSA in Fig.1a during 15-19  
 1293 March 2018. (a) CO (b) OA (c) BC (d) PM<sub>2.5</sub> (e)O<sub>3</sub> (f) OH (g) J(O<sup>1</sup>D), and (h) HCHO

1294

1295 (a)

1296

1297

1298

1299

1300

1301

1302

1303

1304

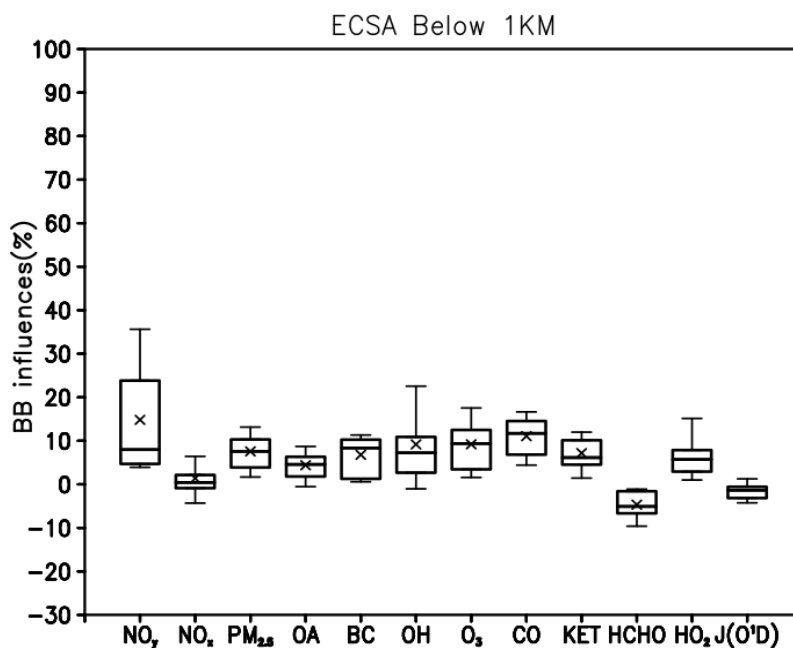
1305

1306

1307

1308

1309



1310 (b)

1311

1312

1313

1314

1315

1316

1317

1318

1319

1320

1321

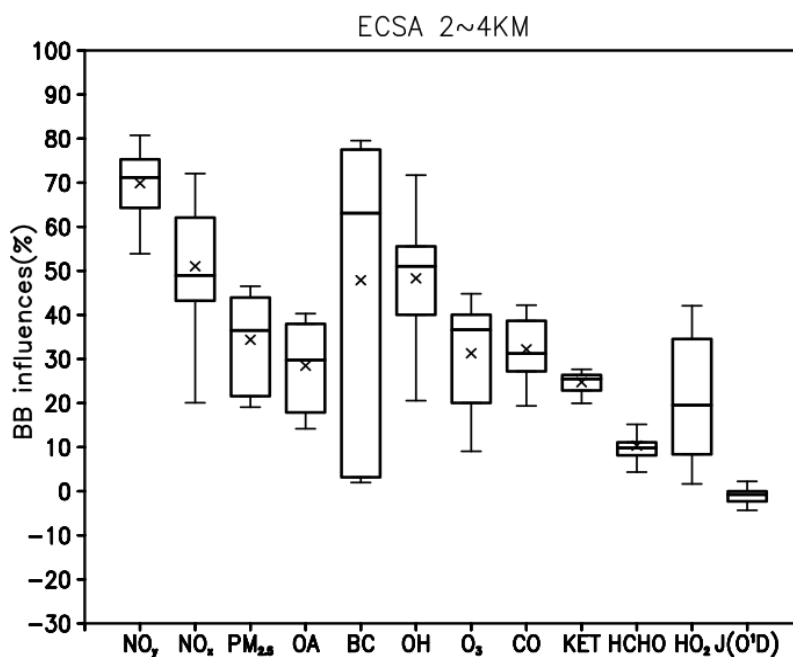
1322

1323

1324

1325

1326



1327 Figure 11 Box plots of simulated BB influences (%) on NO<sub>y</sub>, NO<sub>x</sub>, PM<sub>2.5</sub>, OA, BC, OH,  
1328 O<sub>3</sub>, CO, KET, HCHO, HO<sub>2</sub>, and J(O<sup>1</sup>D) over the region ECSA in Fig. 1a on 17 and 19  
1329 March 2018. (a) below 1 km, (b) between 2 km and 4 km

1330

1331

1332 (a)

1333

1334

1335

1336

1337

1338

1339

1340

1341

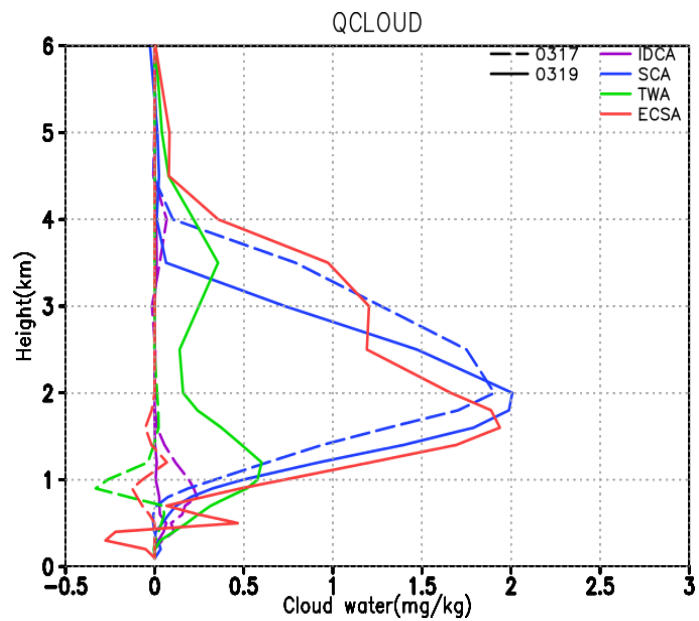
1342

1343

1344

1345

1346



1346

1347 (b)

1348

1349

1350

1351

1352

1353

1354

1355

1356

1357

1358

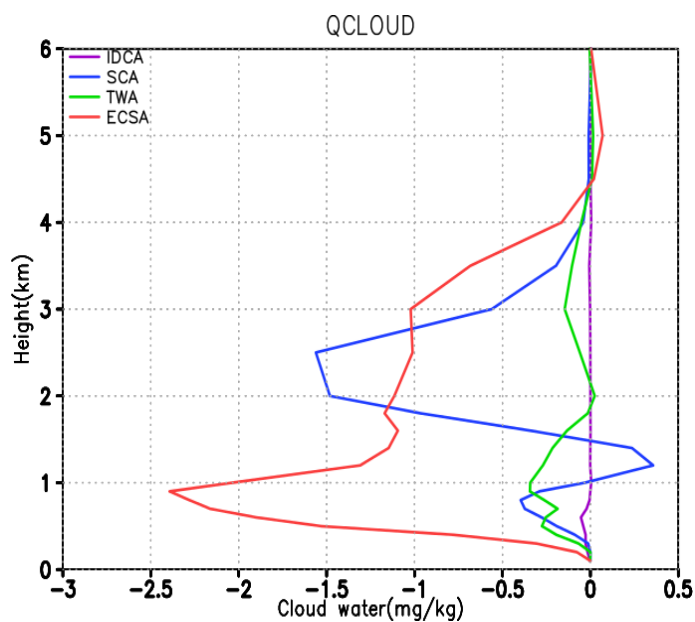
1359

1360

1361

1362

1363



1361

1362

1363

1364 Figure 12 (a) Simulated vertical distribution of BB influences on cloud water difference

1365 between with and without BB emission on 17 (dash) and 19 (solid) March 2018. (b)

1366 Simulated vertical distribution of cloud water difference between with and without

1367 indirect effect in the model on 19 March 2018.

1368 Regions include IDCA, SCA, TWA, and ECSA as shown in Figure 1a.

1369